Title

Potential-based and non-potential-based cohesive zone formulations under mixed-mode separation and over-closure. Part I: Theoretical analysis

Journal

Journal of the Mechanics and Physics of Solids, 63(1)

ISSN

0022-5096

Authors

McGarry, JP
Ó Máirtín, E
Parry, G
et al.

Publication Date

2014-02-01

DOI

10.1016/j.jmps.2013.08.020

Peer reviewed

Journal of the Mechanics and Physics of Solids 63 (2014) 363–385

Contents lists available at ScienceDirect

Journal of the Mechanics and Physics of Solids

journal homepage: www.elsevier.com/locate/jmps

Potential-based and non-potential-based cohesive zone formulations under mixed-mode separation and over-closure—Part II: Finite element applications

Éamonn Ó Máirtín [a], Guillaume Parry [b], Glenn E. Beltz [c], J. Patrick McGarry [a,*]

[a] Mechanical and Biomedical Engineering, College of Engineering and Informatics, National University of Ireland, Galway, Ireland
[b] SIMAP, Institut National Polytechnique de Grenoble, Grenoble, France
[c] Department of Mechanical Engineering, University of California Santa Barbara, Santa Barbara, USA

ARTICLE INFO

Article history:
Received 24 August 2012
Received in revised form
10 June 2013
Accepted 22 August 2013
Available online 11 September 2013

Keywords:
Cohesive Zone
Finite Elements
Buckling
Delamination
Fracture

ABSTRACT

This paper, the second of two parts, presents three novel finite element case studies to demonstrate the importance of normal-tangential coupling in cohesive zone models (CZMs) for the prediction of mixed-mode interface debonding. Specifically, four new CZMs proposed in Part I of this study are implemented, namely the potential-based MP model and the non-potential-based NP1, NP2 and SMC models. For comparison, simulations are also performed for the well established potential-based Xu–Needleman (XN) model and the non-potential-based model of van den Bosch, Schreurs and Geers (BSG model). *Case study 1:* Debonding and rebonding of a biological cell from a cyclically deforming silicone substrate is simulated when the mode II work of separation is higher than the mode I work of separation at the cell-substrate interface. An active formulation for the contractility and remodelling of the cell cytoskeleton is implemented. It is demonstrated that when the XN potential function is used at the cell-substrate interface repulsive normal tractions are computed, preventing rebonding of significant regions of the cell to the substrate. In contrast, the proposed MP potential function at the cell-substrate interface results in negligible repulsive normal tractions, allowing for the prediction of experimentally observed patterns of cell cytoskeletal remodelling. *Case study 2:* Buckling of a coating from the compressive surface of a stent is simulated. It is demonstrated that during expansion of the stent the coating is initially compressed into the stent surface, while simultaneously undergoing tangential (shear) tractions at the coating-stent interface. It is demonstrated that when either the proposed NP1 or NP2 model is implemented at the stent-coating interface mixed-mode over-closure is correctly penalised. Further expansion of the stent results in the prediction of significant buckling of the coating from the stent surface, as observed experimentally. In contrast, the BSG model does not correctly penalise mixed-mode over-closure at the stent-coating interface, significantly altering the stress state in the coating and preventing the prediction of buckling. *Case study 3:* Application of a displacement to the base of a bi-layered composite arch results in a symmetric sinusoidal distribution of normal and tangential traction at the arch interface. The traction defined mode mixity at the interface ranges from pure mode II at the base of the arch to pure mode I at the top of the arch. It is demonstrated that predicted debonding patterns are highly sensitive to normal-tangential coupling terms in a CZM. The NP2, XN, and BSG models exhibit a strong bias towards mode I separation at the top of the arch, while the NP1 model exhibits a bias towards mode II debonding at the base of the arch. Only the SMC model provides mode-independent behaviour in the early stages of

* Corresponding author. Tel.: +35 391 493 165.
E-mail address: patrick.mcgarry@nuigalway.ie (J.P. McGarry).

http://dx.doi.org/10.1016/j.jmps.2013.08.019

debonding. This case study provides a practical example of the importance of the behaviour of CZMs under conditions of traction controlled mode mixity, following from the theoretical analysis presented in Part I of this study.

1. Introduction

Cohesive zone models (CZMs) have been implemented for numerous applications. A large variety of cohesive zone laws have been reported in literature including; polynomial (Tvergaard, 1990), piece-wise linear (Tvergaard and Hutchinson, 1992), exponential (Xu and Needleman, 1993), and rigid-linear cohesive zone laws (Camacho and Ortiz, 1996). A CZM which first provided a phenomenological description of normal separation was developed by Needleman (1987) for analysing void nucleation by inclusion debonding in an elastic-viscoplastic matrix. A trapezoidal form of traction–separation response was used to model the resistance of crack growth following the initiation of a crack at an interface by Tvergaard and Hutchinson (1992). A piece-wise linear softening function was presented by Planas and Elices (1993) for the asymptomatic analysis of a cohesive crack. A rigid-linear law was implemented by Camacho and Ortiz (1996) to investigate the propagation of numerous cracks along random paths in a brittle material. Another study involving a rigid-linear CZM involved a damage-based CZM for simulating fatigue under cyclic loading (Ural et al., 2009).

The Xu–Needleman (XN) CZM was implemented by Abdul-Baqi and Van der Giessen (2001) for the prediction of indentation-induced delamination of an elastic thin film from a ductile substrate. It was reported that delamination initiated primarily in a tangential mode at two to three times the contact radius of the spherical indenter. Bilinear, exponential and trapezoidal CZMs were implemented by Yan and Shang (2009) to predict interfacial delamination in piezoelectric (PZT) thin films. Specifically, the fracture process along the Cr (chromium)/PZT interface was investigated. Modelling delamination of unidirectional fibre composites and adhesive joints, Sørensen et al. developed a mixed-mode cohesive zone from a potential surface using experimental data from double cantilever beam tests with uneven bending moments (Sørensen et al., 2008; Sørensen and Jacobsen, 2009).

While CZMs have been used extensively for a wide array of applications and loading conditions, few studies have rigorously investigated the effect of coupling terms on predicted behaviour, both for displacement and for traction controlled mode mixity. In Part I of this two parts study a thorough theoretical analysis of potential-based and non-potential-based CZMs under conditions of mixed-mode separation and mixed-mode over-closure was presented. Problems are identified with the well established potential-based Xu–Needleman (XN) model (Xu and Needleman, 1993) and a number of new potential-based and non-potential-based models are proposed. In particular, the following was demonstrated for the XN formulation: (i) Repulsive normal tractions are computed during mode II or mixed-mode separation if the work of tangential (mode II) separation (ϕ_t) exceeds the work of normal (mode I) separation (ϕ_n); (ii) Residual normal tractions must be overcome following a complete mode II or mixed-mode separation if ϕ_n exceeds ϕ_t; (iii) If $\phi_t = \phi_n$, incorrect penalisation of mixed-mode over-closure is computed, leading to reduced or repulsive tangential tractions; (iv) Under conditions of traction dependent mode mixity separation paths for the XN model reveal a strong bias toward mode I separation.

A modified potential-based (MP) formulation was proposed in order to partially overcome the limitations of the XN formulation. The MP model reduces the zone in which repulsive or residual tractions occur during mixed-mode separation if the work of normal and tangential separation are unequal. Additionally, the MP model improves upon the over-closure performance of the XN model by providing increased resistance to tangential separation during mixed-mode over-closure. While the MP formulation limits the zone in which non-physical repulsive and residual normal tractions occur, repulsive normal tractions cannot be fully eliminated in a potential-based CZM if $\phi_t \neq \phi_n$. An important consequence of this is that under traction controlled mode mixity when $\phi_t > \phi_n$, potential-based models fail to capture a gradual change from mode II to mode I work of separation, as reported experimentally for traction controlled interface separation (Hutchinson and Suo, 1992).

A non-potential-based formulation was proposed by van den Bosch et al. (2006) (BSG model) in order to provide improved coupling under mixed-mode separation. However, in Part I of this study it was noted that the BSG model does not provide correct penalisation of mixed-mode over-closure. A new non-potential-based formulation (NP1) was proposed in order to obtain correct coupling in both mixed-mode separation and in mixed-mode over-closure. Noting that it is not possible to prescribe identical mode I and mode II separation behaviour for the XN, BSG and NP1 formulations, a second non-potential-based formulation (NP2) was proposed. Identical traction–separation relationships in mode I, mode II and in pure mixed-mode (45°) separation are achieved for this formulation. This formulation also provides correct penalisation of mixed-mode over-closure. However, it was demonstrated that NP2 performs poorly in traction controlled mode mixity, with separation paths ultimately tending towards pure mode I or pure mode II with a singularity for 45° separation. Finally, following from the work of Tvergaard and Hutchinson (1993) a model in which the coupling terms are based on the separation magnitude (SMC model) was considered in order to provide mode-independent behaviour under displacement controlled conditions.

In Part II of this two-part study we present three case studies, each of which represents a novel application of mixed-mode cohesive zone formulations. The first case study entails the simulation of the mixed-mode debonding of a cell from a substrate under cyclic loading when the work of tangential separation exceeds the work of normal separation ($\phi_t > \phi_n$). We demonstrate that physically unrealistic repulsive normal tractions are computed by the XN model during mixed-mode separation of the cell from the substrate. When the proposed MP model is used, computed repulsive normal tractions are shown to be negligible. Using an active bio-chemo-mechanical model for stress fibre remodelling in the cell cytoplasm (Deshpande et al., 2006), we demonstrate that incorrect mixed-mode behaviour at the cell interface can significantly affect the predicted distribution of contractile cytoskeleton.

In the second case study we consider the behaviour of a coating on the compressive region of a cardiovascular stent during expansion of the stent. We demonstrate that the non-potential-based BSG model fails to correctly penalise mixed-mode over-closure of the coating into the stent surface, leading to an under-prediction of coating buckling on the compressive surface of the stent. The NP1 and NP2 models proposed in the present study correctly penalise mixed-mode over-closure, leading to the simulation of significant coating buckling.

In the third case study we consider the problem of debonding at the interface of a bi-layered arch. We present a recently developed analytical solution for the stress state at the arch interface, demonstrating symmetry between shear and normal tractions, with the interface traction magnitude being constant along the interface. We then analyse the ability of the potential and non-potential-based CZMs to replicate the analytical solution and we demonstrate that the normal-tangential coupling terms in a cohesive zone formulation can significantly affect computed debonding patterns at the arch interface.

2. Case studies

2.1. Case study I—Modelling cell-substrate interface delamination

Several in-vitro studies have investigated the response of cells to cyclic stretching. For example, in the study of Wang et al. (1995), human melanocytes were grown on rectangular culture dishes which were subjected to unidirectional cyclic stretching at a frequency of 1 Hz for 24 h. It was reported that the cells aligned in the direction of minimum strain.

In the study of Wang et al. (2001), human endothelial cells were seeded on deformable silicone membranes. The cells were subjected to three types of cyclic stretching; simple elongation, pure uniaxial stretching and equi-biaxial stretching. In all cases, it was reported that the cells aligned in the direction of minimum substrate strain. This study also revealed that the rate and extent of early cell reorientation depended mostly on the stretching magnitude and not on the stretch frequency. Similarly in the work of Balestrini et al. (2010), dermal fibroblasts aligned in a direction away from the direction of principal strain when seeded on flexible-bottomed culture wells. These studies suggest that cells reorient to minimise the strain acting on them. However, the specific mechanisms involved to produce such behaviour are not well understood.

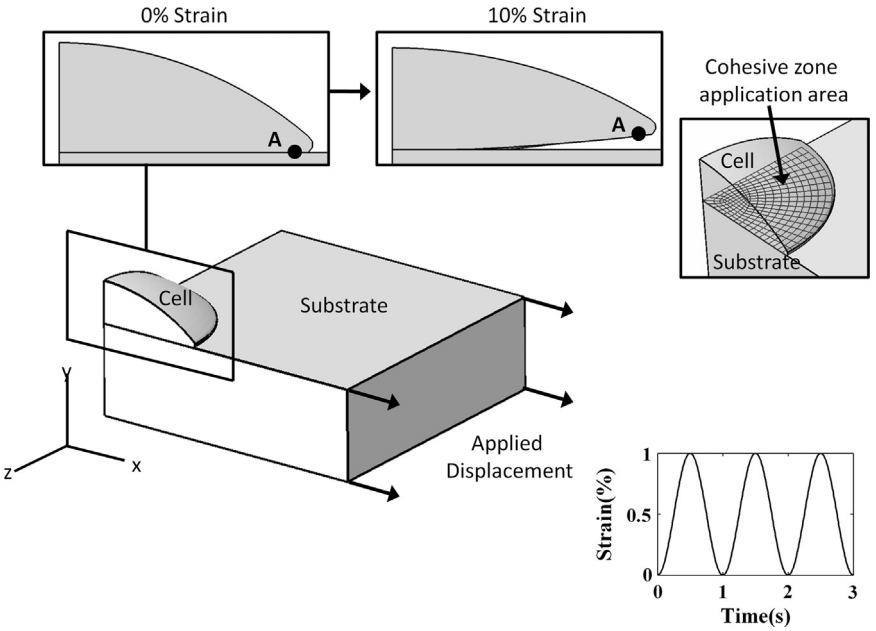

Fig. 1. Geometry of cell and substrate model. Arrows indicate the direction of cyclic substrate deformation. The inserts show the deformed geometry of the cell at 10% strain. Point A indicates a node at the cell-substrate interface where mixed-mode separation is computed. The cohesive zone application area is also highlighted.

In this study the biomechanical response of a cell on a cyclically stretching silicone substrate is simulated (Fig. 1). It is demonstrated that mixed-mode separation occurs at the cell-substrate interface when the work of tangential separation exceeds the work of normal separation ($\phi_t > \phi_n$). In particular, it is demonstrated that the use of the XN model at the cell-substrate interface results in the computation of repulsive normal tractions. Further, it is demonstrated that the MP model, proposed by the authors, significantly decreases the computation of such non-physical repulsive tractions. A three-dimensional active stress fibre formulation (Deshpande et al., 2006; Ronan et al., 2012) is used to simulate active remodelling and contractility of the cell cytoplasm. Simulations reveal that incorrect treatment of mixed-mode behaviour at the cell-substrate interface has a significant effect on prediction of stress fibre remodelling in the cell cytoplasm.

2.1.1. Finite element model

The cell geometry, shown in Fig. 1, is based on the experimental data of Caille et al. (2002) for endothelial cells. Cells are attached to a silicone substrate which is cyclically stretched from 0% to 10% nominal axial strain via a sinusoidally varying displacement boundary condition at a frequency of 1 Hz, based on experimental boundary conditions (Wang et al., 1995; Wang et al., 2001; Moretti et al., 2004; Kaunas et al., 2005; Na et al., 2007; Hsu et al., 2009). One quarter of the cell and substrate geometries are modelled due to the use of symmetry boundary conditions. The silicone substrate is assumed to behave as a linear elastic material with a Poisson's ratio of 0.4 and a Young's modulus of 0.25 MPa (McGarry et al., 2005).

Cohesive zone formulations are used to simulate the cell-substrate interface. Specifically, the XN and MP formulations are considered. The CZMs are implemented in Abaqus Standard software (V.6.8-1, Abaqus Inc., RI, USA) via a user-defined interface subroutine (UINTER). Characteristic interface lengths of $\delta_n = 25\ nm$ and $\delta_t = 35.36\ nm$ are assumed based on ligand–receptor bond lengths reported in literature (Chan et al., 1999; Dong and Lei, 2000). A mode I interface strength of $\sigma_{max} = 4\ \ kPa$ is chosen based on experimental measurements of bond strength and bond density (Thoumine et al., 2000). It is assumed that the mode II strength is higher than mode I strength at the cell-substrate interface, so that $\tau_{max} = 20\ \ kPa$ (corresponding to $q \approx 3$ for the XN model). The exponential shape of the normal traction–separation curve for the three models considered in this case study (XN and MP formulations) is similar to an experimentally measured force-deformation curve for an isolated ligand–receptor bond (Leckband and Israelachvili, 2001), providing motivation for the use of such models at the cell-substrate interface. It is worth noting that traction–separation relationship under pure mode I and pure mode II conditions is identical for both cohesive zone formulations. Critically, however, differences between the mixed-mode behaviour of the models has a pronounced effect on predicted cell debonding, and consequently on cell remodelling.

2.1.2. Constitutive formulation for the active behaviour of the cell actin cytoskeleton

The actin cytoskeleton, which comprises of contractile stress fibres, plays a critical role in the active bio-mechanical behaviour of a cell. Stress fibres are formed in response to signalling cascades in the cell cytoplasm which lead to the assembly of the phosphorylated myosin and polymerised actin filaments. Cross-bridge cycling between the myosin motor proteins and actin filaments generates active contractility in the actin cytoskeleton. Several experimental studies have demonstrated that a reduction in cell tension leads to the dissociation of stress fibres (Franke et al., 1984; Kolega, 1986; Burridge and Chrzanowska-Wodnicka, 1996; Tan et al., 2003; Thomopoulos et al., 2005).

In the present case study, an active bio–chemo-mechanical model proposed by Deshpande et al. (2006) is used to simulate the formation, remodelling and contractility of the actin cytoskeleton. Using a three-dimensional (3D) numerical implementation of this framework developed by Ronan et al. (2012), stress fibre formation at each integration point in the cell cytoplasm is computed in 400 evenly spaced directions in 3D space. Each discrete direction is defined by two angles ω and γ. Theoretically stress fibres can form in an infinite number of directions at any point in the cell, but it has been demonstrated that a converged solution is obtained when the number of directions considered is greater than 200 (Ronan et al., 2012).

The signal-induced formation and tension-dependent dissociation of the stress fibres is governed by a first order kinetic Eq. (1) in terms of the dimensionless stress fibre activation level, η (Deshpande et al., 2006).

$$\dot{\eta}(\gamma,\omega) = [1-(\eta(\gamma,\omega))] = Ck_f - \left[1-\frac{\sigma(\gamma,\omega)}{\sigma_0(\gamma,\omega)}\right](\eta(\gamma,\omega))k_b \tag{1}$$

The first term on the right hand side drives the assembly of a stress fibre in response to a time dependent signal, C. k_f is a forward reaction rate constant. The second term drives the dissociation of the stress fibre when the stress fibre tension, $\sigma(\gamma,\omega)$ is lower than the isometric tension, $\sigma_0(\gamma,\omega)$. k_b is the backwards reaction rate constant. The isometric tension is proportional to the stress fibre activation level, such that;

$$\sigma_o(\gamma,\omega) = \Sigma_{\max}\eta(\gamma,\omega) \tag{2}$$

where the model parameter Σ_{max} represents the isometric tension of a fully activated stress fibre. As previously stated, stress fibre tension is generated by the cross-bridge cycling of actin-myosin pairs (Warshaw et al., 1990) resulting in a contractile behaviour similar to that of skeletal muscle. This behaviour is captured using the following Hill-like relation between stress

fibre tension $\sigma(\gamma,\omega)$ and strain rate $\dot{\varepsilon}(\gamma,)$;

$$\frac{\sigma(\gamma,\omega)}{\sigma_0(\gamma,\omega)}=\begin{cases}0 & \frac{\dot{\varepsilon}(\gamma,\omega)}{\dot{\varepsilon}_0}<-\frac{\eta(\gamma,\omega)}{k_v}\\ 1+\frac{k_v}{\eta(\gamma,\omega)}\frac{\dot{\varepsilon}(\gamma,\omega)}{\dot{\varepsilon}_0} & -\frac{\eta(\gamma,\omega)}{k_v}\le\frac{\dot{\varepsilon}(\gamma,\omega)}{\dot{\varepsilon}_0}\le 0\\ 1 & \frac{\dot{\varepsilon}(\gamma,\omega)}{\dot{\varepsilon}_0}>0\end{cases} \tag{3}$$

where the model parameters k_v and $\dot{\varepsilon}_0$ determine the slope of the Hill curve (Hill, 1938). It should be noted that stress fibres yield when lengthening ($\dot{\varepsilon}_0>0$). This active formulation is placed in parallel with a passive hyperelastic material model which represents the non-contractile elements of the cell cytoplasm, including intermediate filaments and microtubules. This framework has been experimentally validated for a range of cell phenotypes (Dowling et al., 2012; McGarry et al., 2009; Weafer et al., 2013). Material parameters for the active and passive components of the cell material model are taken from Mcgarry et al., (2009) and Ronan et al. (2012).

In summary, a signal C leads to the formation of a contractile stress fibre bundle. If the stress fibre is fully activated ($\eta=1$) it will produce a maximum isometric tension, Σ_{max}. If the stress fibre shortens, either due to its own contractile action or due to an externally applied load, its tension–velocity relationship is based on the classical actin–myosin cross-bridge cycling model (Eq. (3)). When the fibre lengthens due to an external load, it yields, producing a tension equal to the isometric value for all lengthening velocities. When the stress fibre shortens, the associated reduction in tension leads to dissociation of the stress fibre, thus lowering the activation level, η. In the current case study, prevention of reattachment of the cell to the substrate due to repulsive normal interface tractions results in a reduced stress fibre shortening rate during substrate unloading and hence a reduced dissociation rate. Hence, correct mixed-mode interface behaviour is critical for the prediction of stress fibre remodelling in the cell during cyclic substrate deformation.

2.1.3. *Case study I: results*

Fig. 2 shows the evolution of normal traction, (T_n) and separation, (Δ_n) at a point A (Fig. 1) at the leading edge of the cell during the first five substrate cycles. As the substrate is stretched, nodes at the front of the cell undergo mixed-mode debonding, as illustrated for point A in Fig. 1. Firstly, considering the results computed by the XN model (Fig. 2(a)): During the first cycle, point A undergoes mixed-mode separation with the normal traction increasing up to a value of $T_n\approx 0.9\sigma_{max}$ and then decreasing as the node fully debonds (pure mode I debonding would result in a higher peak normal traction of $T_n=\sigma_{max}$). A repulsive traction is computed for a brief period. The normal traction then vanishes and the normal separation undergoes a rapid increase to a peak value of $\sim 30\delta_n$ when the substrate is fully stretched to 10% nominal strain. As the substrate stretch decreases during the second half of the cycle the normal separation decreases. However, the cell surface at point A does not return to the substrate at the end of the cycle, with a separation of $\sim 5\delta_n$ being computed when the substrate returns to 0% nominal strain. Clearly, in Fig. 2(a), this end of cycle separation ($\Delta_n>0$) is accompanied by repulsive normal tractions ($T_n<0$). As detailed in Part I of this study, such repulsive normal tractions can be computed in potential-based models under mixed-mode conditions if the work of tangential separation exceeds the work of normal separation ($\phi_t>\phi_n$). As the substrate stretching resumes at the start of the second cycle the repulsive traction disappears, but it should be noted that the peak traction during the stretching phase of the second cycle is considerably lower than that of the first cycle as the node is already partially debonded due to the computation of repulsive forces at the end of the first cycle. As highlighted in Fig. 2(a), repulsive tractions prevent the cell from contacting the substrate at point A at the end of every subsequent cycle.

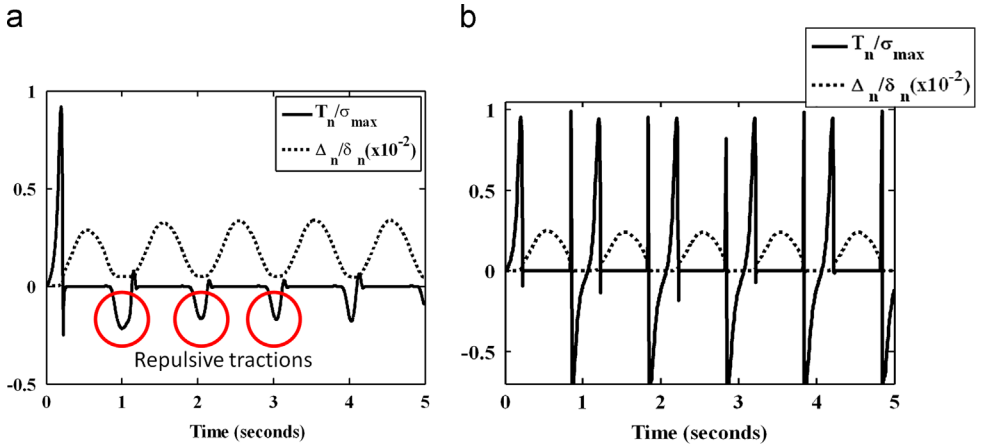

Fig. 2. Normal traction (T_n/σ_{max}) and normal separation (Δ_n/δ_n) as a function of time for (a) the XN and (b) MP ($m=1$) cohesive zone models. Repulsive normal tractions are highlighted in the case of the XN model.

Tractions and separations at point A computed using the MP model (Fig. 2(b)) reveal a markedly different pattern to those computed using the XN model. During the initial substrate stretching in the first cycle the behaviour is almost identical to the XN predictions with normal traction increasing up to a value of $T_n \approx 0.9\sigma_{max}$ and then decreasing, marking the onset of mixed-mode debonding. Following debonding, a small repulsive force ($T_n \approx -0.05\sigma_{max}$) is computed for a brief period after which the traction disappears and the normal separation rapidly increases until the substrate is fully stretched. During the second half of the first cycle, when the substrate strain is reduced from 10% to 0%, point A returns to the substrate surface. As no damage is included in the model, the node rebonds in a mixed-mode fashion, with a peak normal traction of $T_n \approx 0.9\sigma_{max}$ being computed during rebonding. At the end of the cycle point A contacts the substrate surface and then slightly overcloses into the substrate. This over-closure is appropriately penalised by negative normal tractions. It is important that such negative normal tractions which penalise (negative) normal over-closure are not confused with the repulsive negative normal tractions computed by the XN model in Fig. 2(a) at the end of the cycle when a positive normal separation is computed. During the second and subsequent cycles for the MP model (Fig. 2(b)), point A goes through a similar debonding and rebonding cycle, with peak tractions of $T_n \approx 0.9\sigma_{max}$ being computed twice per cycle and extremely small repulsive tractions being computed only for a brief period following nodal debonding.

Fig. 2 presents traction and separation history for a single node at the leading edge of the cell. Fig. 3 reveals the full extent of repulsive normal tractions computed by the XN model. Specifically, Fig. 3(a)–(c) shows the computed normal tractions, normal displacements and effective tangential tractions computed at the cell-substrate interface for the XN and MP models

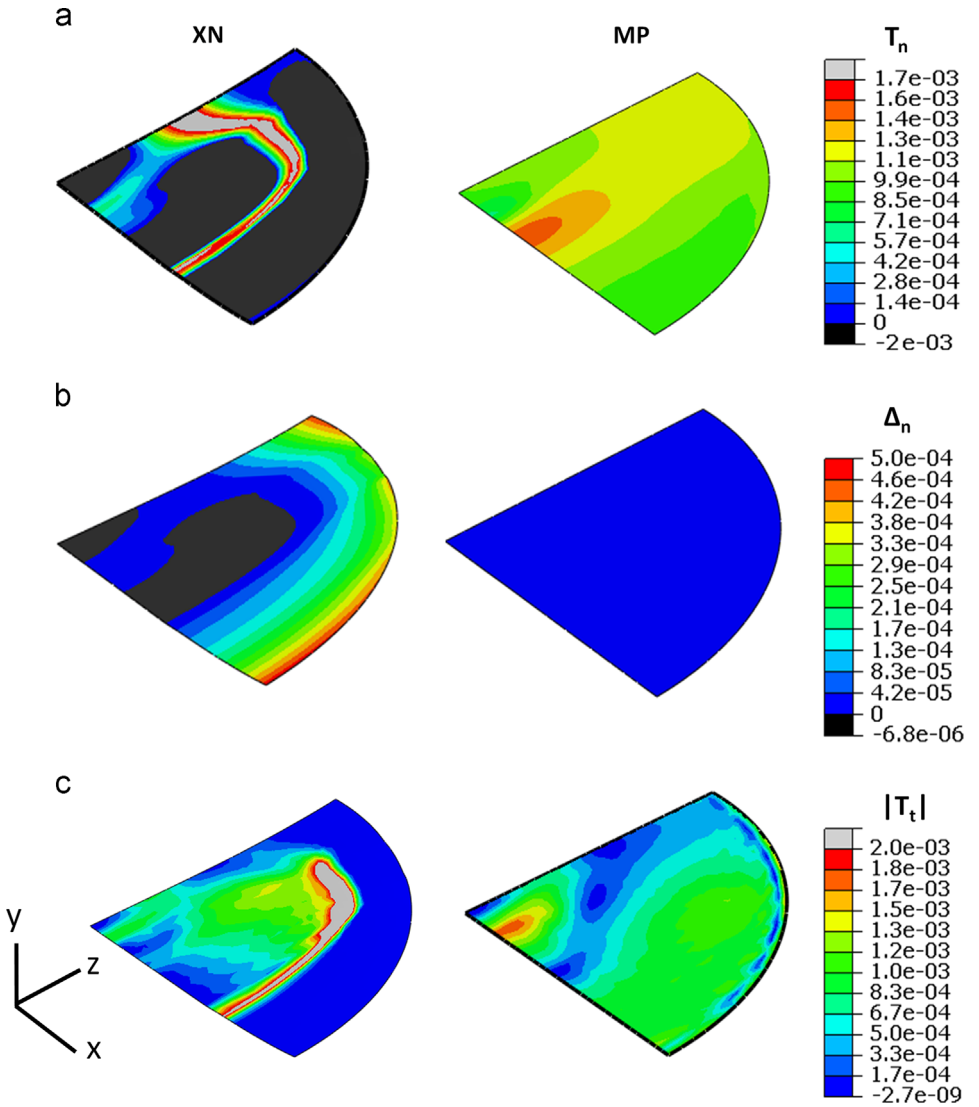

Fig. 3. (a) Computed normal tractions (T_n); (b) Computed normal displacements (Δ_n); (c) Computed effective tangential tractions ($|T_t|$) for XN and MP ($m=1$) cohesive zone models. Results are shown at 0% substrate strain following 3 substrate strain cycles. (For interpretation of the references to colour in this figure, the reader is referred to the web version of this article.)

at the end of the third cycle when the substrate has returned to 0% nominal strain. In the case of the XN model, significant regions of unphysical repulsive normal tractions are computed around the outer perimeter of the contact region (characterised as regions where positive normal separations are coincident with negative normal tractions, as distinct from regions in which over-closure is being penalised, where both normal separations and normal tractions are negative). In contrast, no unphysical repulsive normal tractions are computed for the MP model when the substrate returns to 0% nominal strain and normal separations are close to zero throughout the interface, indicating a complete re-adhesion of the cell to the substrate. As can be seen in Fig. 3(c), the repulsive normal tractions in the XN simulation have a pronounced affect on the tangential tractions at the cell-substrate interface, with minimal computed tractions at the leading edge of the cell at 0% nominal substrate strain. In contrast, tangential tractions are computed at the leading edge of the cell for MP following full cell reattachment.

Fig. 4 shows the predicted remodelling of stress fibres at the base of the cell over 30 loading cycles using the MP model. Prior to initiation of cyclic substrate stretching an equilibrium stress fibre distribution is computed in response to an exponentially decaying signal in the cell cytoplasm on a static substrate. As expected, in the absence of applied external substrate loading, an axisymmetric stress fibre distribution occurs in the cell (Fig. 4(a)). No debonding occurs during this stage of the simulation as the interface tractions generated by the contractile actin cytoskeleton are an order of magnitude lower than the interface strength. Subsequent cyclic substrate stretching in the x-direction results in cyclic debonding

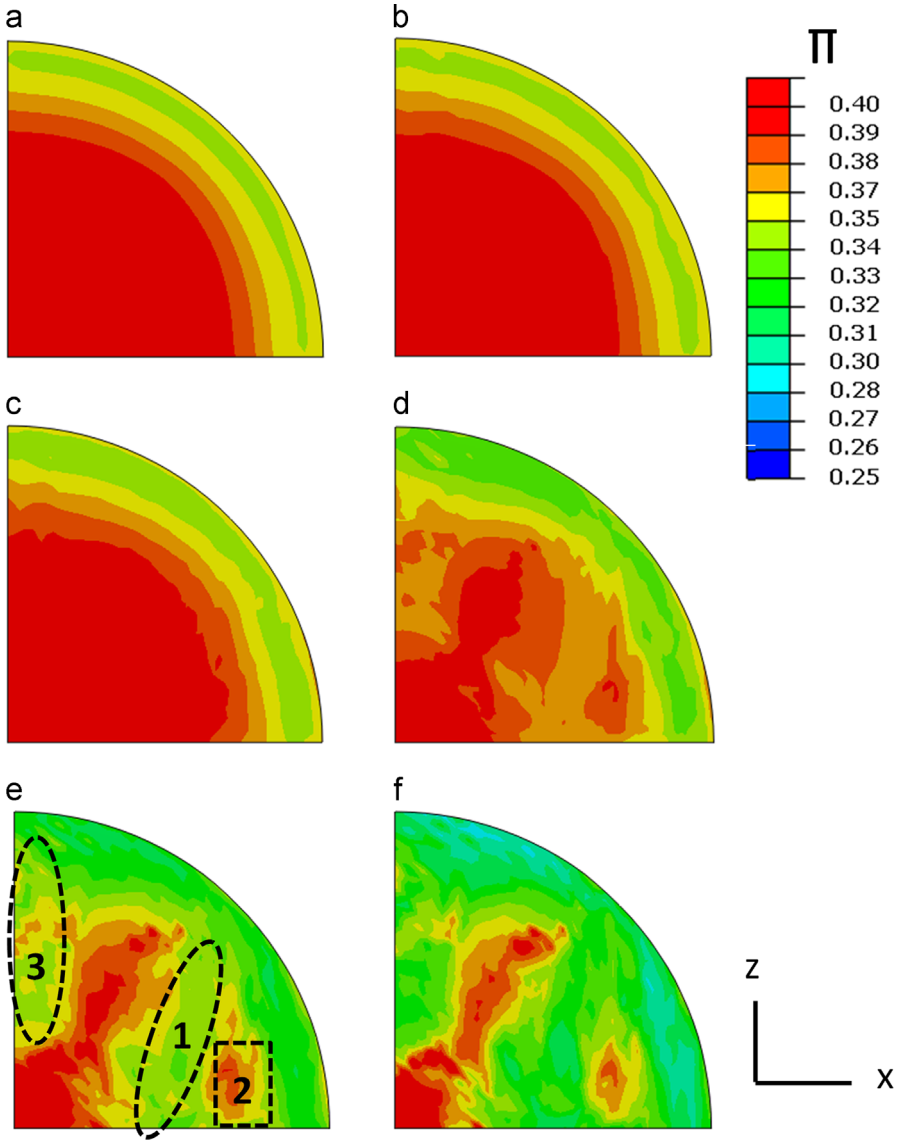

Fig. 4. Computed dominant stress fibre bundling direction at the cell interface surface for the MP model following (a) equilibrium; (b) 1 cycle; (c) 3 cycles; (d) 10 cycles; (e) 20 cycles and (f) 30 cycles.

and rebonding of significant regions of the cell-substrate interface (as shown in Fig. 2) but little change in stress fibre distribution following one and three cycles (Fig. 4(b and c)). However, following 10 cycles (Fig. 4(d)) it can be observed that stress fibre dissociation begins to occur. A clear pattern of stress fibre redistribution emerges following 20 cycles (Fig. 4(e)), whereby stress fibres remain intact in the regions of lowest cyclic strain rate. In highlighted region 1, stress fibre shortening in the x-direction during the unloading half cycle results in tension reduction and dissociation. It should be noted that region 2 debonds during substrate stretching and reattaches to the substrate towards the end of the unloading half cycle (as shown in Fig. 2(b)). Therefore stress fibres in this region experience a reduced period of shortening and tension reduction during unloading half cycles, leading to a slower rate of dissociation. Region 3 undergoes stress fibre shortening in the z-direction during cell stretching due to the Poisson's effect, leading to dissociation. By 30 cycles (Fig. 4(f)) a distinct band of stress fibres are computed from the centre of the cell to the cell periphery at an angle of $\sim 70^\circ$ to the stretching (x) direction. Further dissociation is also computed in region 2 following 30 cycles, all be it at a slower rate due to debonding and rebonding. The prediction that stress fibres align at $\sim 70^\circ$ is strongly supported by experimental findings (Wang et al., 1995; Wang et al., 2001; Kaunas et al., 2005), as shown in Fig. 5. This direction corresponds to the direction of minimum strain rate for a silicone substrate with a Poisson's ratio of 0.4. This pattern of stress fibre alignment is not predicted by the XN model,

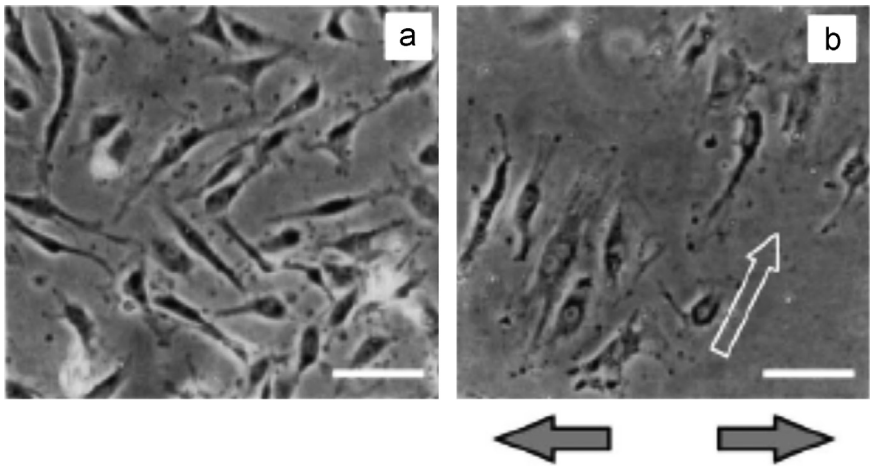

Fig. 5. Experimental image of endothelial cell alignment in response to cyclic stretching (right). Prior to stretching cells were randomly aligned (left). Adapted from Wang et al. (2001).

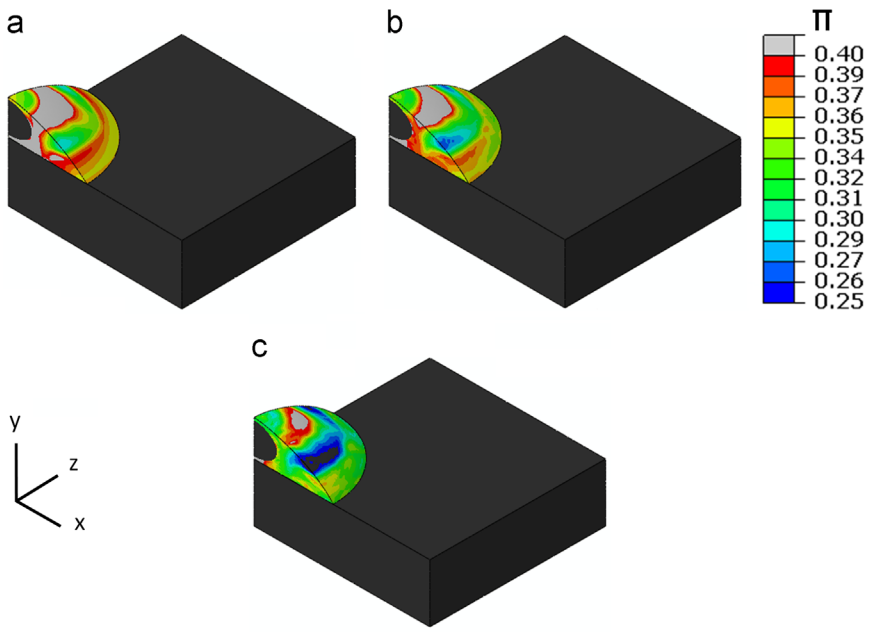

Fig. 6. Computed dominant stress fibre bundling direction in the cell geometry for the MP model following (a) equilibrium; (b) 10 cycles and (c) 30 cycles.

as repulsive normal tractions during the unloading half cycles prevents reattachment of the cell to the substrate, as shown in Fig. 2(a). Therefore stress fibres in region 3 are not subjected to shortening during any period of the unloading half cycles and no dissociation occurs in this region. Fig. 6 demonstrates that significant stress fibre remodelling occurs throughout the entire cell cytoplasm, and not just at the base of the cell as shown in Fig. 4.

It is worth noting that the use of potential-based models for the cyclic debonding and rebonding of the cell ensure that the weak criterion for positive dissipation is satisfied, i.e. zero net dissipation occurs when the cell rebonds to the substrate at the end of a loading cycle. As shown in Part I of this study, the strong criterion for positive dissipation is not necessarily satisfied by the non-potential formulations, i.e. instantaneous dissipation will not at all times be positive. However, for the complex interaction between a cell and substrate, instantaneous negative dissipation may well be appropriate during cell-substrate rebonding.

In summary, this case study demonstrates the advantages of the proposed MP CZM for simulations that involve mixed-mode delamination and readhesion. Significant regions of repulsive normal tractions at the cell-substrate interface are computed by the XN model, preventing the readhesion of the cell to the substrate during substrate unloading half-cycles. The implications of the computation of unphysical repulsive forces are clearly demonstrated in terms of predicting changes in contact between the cell and the substrate and remodelling of the actin cytoskeleton. The simulations suggest that alignment of the actin cytoskeleton has occurred by 30 cycles. Such alignment is typically observed in experimental studies following more than 3600 cycles (one hour of cycling at 1 Hz) (Wang et al., 1995; Wang et al., 2001; Kaunas et al., 2005). The predicted rate of alignment can be altered by decreasing the reaction rate constants, k_f and k_b, in Eq. (1). However, the simulation of such a large number of cycles is not computationally feasible using the highly nonlinear 3D active stress fibre formulation. The accelerated remodelling of the cell actin cytoskeleton in the present study provides a prediction of the remodelling pattern of the actin cytoskeleton. Experimental studies demonstrate that following $\sim$10,000 cycles both the actin cytoskeleton and the cell morphology align in the direction of minimum substrate strain as discussed in Section 2.1 above. For silicon substrates this corresponds to $\sim 70^\circ$ (as dictated by a substrate Poisson's ratio of $\sim$0.4).

The simulation of the active contractility of the actin cytoskeleton represents a significant advance on previous cell debonding simulation, in which the cell is assumed to behave as a passive viscoelastic material (McGarry et al., 2005; McGarry and McHugh, 2008). Stress fibre remodelling due to dynamic loading is not just important for an endothelial cell, but also for chondrocytes embedded in cartilage tissue, as investigated in the computational study of Dowling et al. (2013). However, the modelling of the cell-substrate interface using a passive cohesive zone framework still represents a significant simplification. Cell-substrate adhesion entails traction-dependent binding of high-affinity integrins to ligands, leading to focal adhesion assembly, as detailed in the thermodynamically consistent framework of Deshpande et al. (2008).

Additionally, the kinetics of bond formation and rupture has been the subject of a number of studies (Bell, 1978; Evans, 1985; Dembo et al., 1988; Dong and Lei, 2000; Freund and Lin, 2004). As the focus of the present case study is on the mixed-mode behaviour of path-independent potential-based models, the cell-substrate interface is treated as a passive entity, with debonding and readhesion being governed exclusively by an interface potential. The implementation of a mixed-mode active cell-substrate interface model is beyond the scope of the present case study and has recently been reported elsewhere (Ronan et al., in press).

2.2. Case study II-modelling stent-coating interface delamination

Several experimental studies have reported buckling of stent coatings in compressive regions during stent deployment (Regar et al., 2001; Basalus and von Birgelen, 2010). While the study of Hopkins et al. (2010) simulated delamination and buckling of compliant polymer coatings during deployment, no study to date has modelled the behaviour of stiffer metallic and ceramic coatings on stent surfaces, despite the extensive use of such coatings to improve stent biocompatibility (Babapulle and Eisenberg, 2002; Edelman et al., 2001; Windecker et al., 2001). In this case study the mechanical behaviour of a titanium coating on the compressive region of a stent surface is simulated during stent deployment. The BSG, NP1 and NP2 formulations are used to model the stent-coating interface. Our simulations reveal that in regions where the coating is compressed into the stent surface while simultaneously undergoing tangential (shear) tractions at the coating-stent interface, the NP1 and NP2 formulations provide a correct penalisation of mixed-mode coating over-closure (compression) during deployment, leading to buckling of the coating from the stent surface. In contrast, the BSG formulation does not penalise mixed-mode coating over-closure, leading to the computation of incorrect interface traction, coating stress, and consequently a significant reduction of coating buckling.

2.2.1. Finite element model Parameters

The stent and coating geometry is shown in Fig. 7. A 2D unit cell idealisation is utilised (McGarry et al., 2004) and stent deployment is simulated by imposing displacement boundary conditions on the strut ends. 316 L stainless steel elastic–plastic material properties are assumed for the stent (Young's modulus 200 GPa; Yield stress 264 MPa; Ultimate tensile strength 595 MPa) (McGarry et al., 2007). The titanium coating is assigned the properties of a porous titanium alloy $TiNO_x$ (Young's modulus 92 GPa; Yield stress 702.5 MPa; Ultimate tensile strength 756.5 MPa) (Asaoka et al., 1985). An interface strength of $\tau_{max} = \sigma_{max} = 50$ MPa is used for each CZM and interface characteristic distances are chosen so that peak tractions occur at a separation of 25 nm in both mode I and mode II separation.

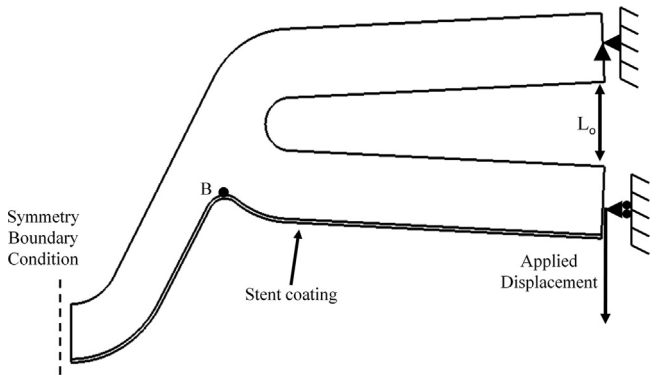

Fig. 7. Geometry of the stent and stent coating. Boundary conditions and applied displacement are highlighted. Point B indicates a node at the stent-coating interface in the compressive region of the stent. The initial circumferential strain (L_o) is also indicated.

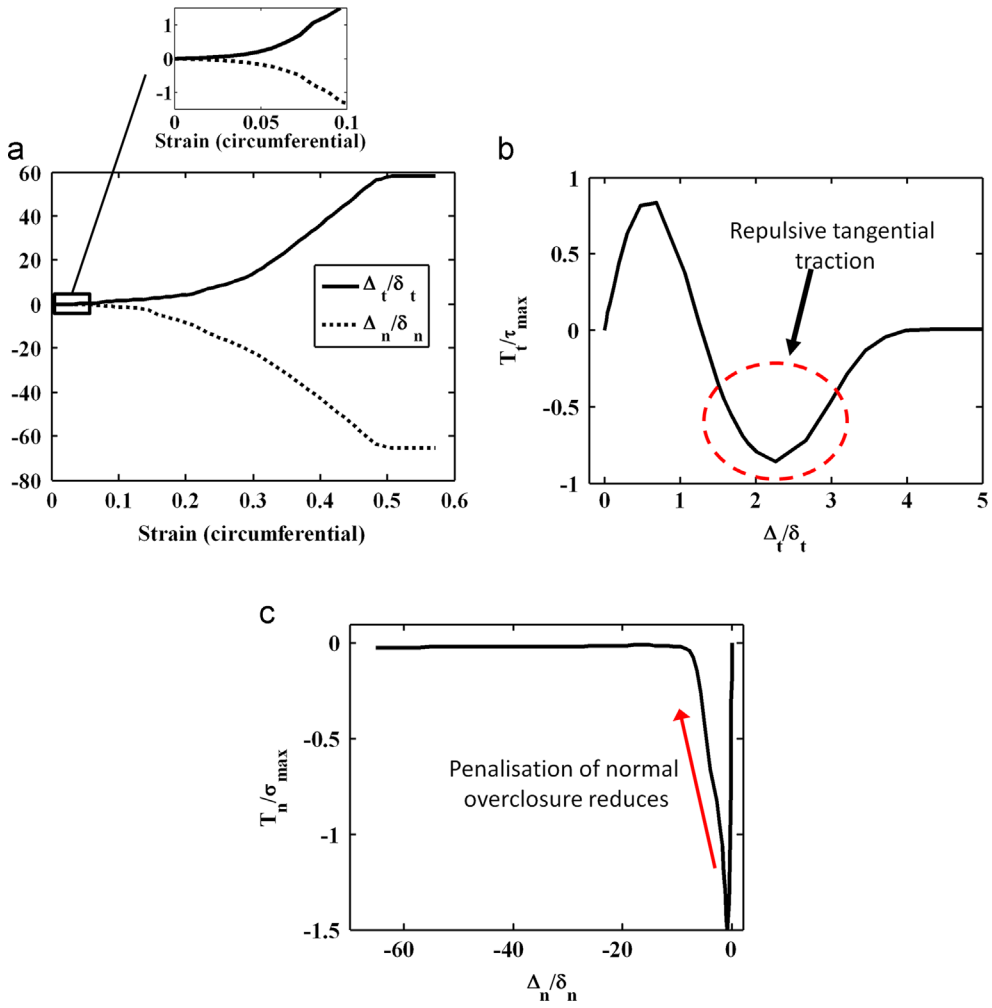

Fig. 8. Interface behaviour computed at point B during stent deployment using the BSG model: (a) Normal (Δ_n/δ_n) and tangential (Δ_t/δ_t) separation as a function of circumferential strain. (b) Tangential traction (T_t/τ_{max}) as a function of tangential separation (Δ_t/δ_t). (c) Normal traction (T_n/σ_{max}) as a function of normal separation (Δ_n/δ_n). (For interpretation of the references to colour in this figure, the reader is referred to the web version of this article.)

2.2.2. *Case study II: results*

Using the BSG formulation at the stent-coating interface, Fig. 8(a) shows the computed normal and tangential separation of a point B at the coating-stent interface (see Fig. 7) during stent deployment. The level of deployment is characterised as the circumferential strain of the stent, simply calculated as $(L-L_o)/L_o$, as shown in Fig. 7. At the curved section in the region

of point B the coating is compressed into the stent surface during deployment. Using the BSG model this results in the computation of mixed-mode coating over-closure characterised by negative normal separations and non-zero tangential separations, as shown in Fig. 8(a). It can be seen that normal over-closure reaches very unrealistic levels ($\Delta_n/\delta_n \approx 60$) during the simulation. Fig. 8(b) shows the corresponding tangential traction–separation relationship. Initially, tangential tractions increase during over-closure at the interface. However, a peak value of tangential traction that is lower than τ_{max} is reached, demonstrating the weakened resistance of the interface to tangential separation during mixed-mode over-closure. Following the peak, tangential traction reduces and becomes negative, despite the tangential separation being positive. This means that, instead of penalising the movement of nodes during mixed-mode over-closure, repulsive tangential tractions encourage increasing tangential separation, despite the coating being overclosed into the substrate. Fig. 8(c) shows the corresponding normal traction–separation behaviour at point B during stent deployment. Initially, normal over-closure is correctly penalised. However, the computation of negative (repulsive) tangential tractions (Fig. 8(b)) reduces the penalisation of normal over-closure at the interface. Therefore, further over-closure at the stent-coating interface is predicted. This unphysical behaviour occurs because repulsive tangential tractions are computed by the BSG model for significant mixed-mode over-closure ($\Delta_n/\delta_n < -1$) as discussed in Part I of this study. Such repulsive tangential tractions lead to excessive tangential separations at the interface, which in turn reduce the penalisation of normal over-closure, leading to excessive mixed-mode over-closure. The failure of the BSG model to penalise mixed-mode over-closure cannot be ameliorated by decreasing the interface characteristic length, with similar results being computed for $\delta_n = 12.5$ nm and $\delta_n = 6.25$ nm. As demonstrated in Part I of this study, similar problems occur for the XN model during mixed-mode over-closure.

Results computed using the NP1 model at the stent-coating interface are shown in Fig. 9. During initial stages of stent deployment, mixed-mode over-closure is computed at point B (Fig. 7) during stent deployment with negative normal separation and non-zero tangential separation (highlighted in the insert of Fig. 9(a)). However, in contrast to the BSG model,

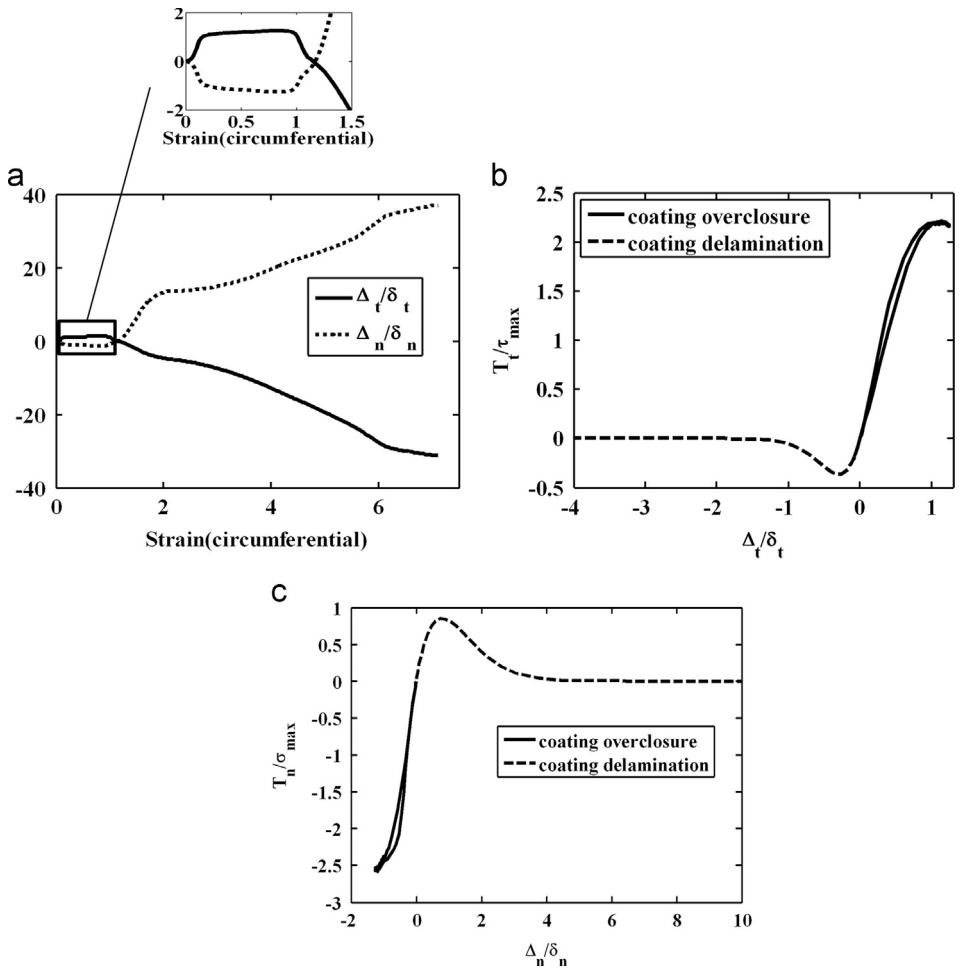

Fig. 9. Interface behaviour computed at point B during stent deployment using NP1: (a) Normal (Δ_n/δ_n) and tangential (Δ_t/δ_t) separation as a function of circumferential strain. (b) Tangential traction (T_t/τ_{max}) as a function of tangential separation (Δ_t/δ_t). (c) Normal traction (T_n/σ_{max}) as a function of normal separation (Δ_n/δ_n).

significant normal over-closure is prevented due to the ability of the NP1 model to penalise mixed-mode over-closure. The correct penalisation of mixed-mode over-closure in the compressive region of the stent results in buckling of the coating. This buckling initiates to the right of point B. Further stent deployment leads to an increase in the buckling region. When a circumferential strain of 1.25 is reached point B is incorporated into the buckling region, as characterised by a change from normal over-closure to normal separation. The prediction of such buckling is dependent on the correct treatment of tangential traction during over-closure. The tangential traction–separation plot during stent deployment is shown in Fig. 9(b). As coating over-closure increases during the initial stages of stent deployment, an increase in tangential separation is penalised by a sharp increase in tangential traction. When normal over-closure begins to decrease due to coating buckling a peak in tangential traction of $T_t/\tau_{max} \approx 2.2$ is computed. As point B enters the regime of normal separation following extensive buckling the tangential movement of the node changes direction, with debonding occurring following a peak traction of $T_t/\tau_{max} \approx -0.3$ at a tangential separation of $\Delta_t/\delta_t \approx -0.2$, as illustrated by the broken line in Fig. 9(b). The increase in resistance to tangential separation during normal over-closure and the decrease in resistance to tangential separation during normal separation that is provided by the NP1 model is physically realistic and is critical for the prediction of coating buckling. For completeness, the normal traction–separation plot during stent deployment is shown in Fig. 9(c). Again this illustrates that NP1 correctly penalises mixed-mode over-closure during initial stages of stent deployment and then correctly predicts mixed-mode separation as the coating buckles during higher deployment, with a reduced peak normal traction of $T_n/\sigma_{max} \approx 0.75$ being computed.

A similar pattern of mixed-mode behaviour at point B is predicted by the NP2 model, as shown in Fig. 10. Again, mixed-mode over-closure is computed at point B during early stages of stent deployment (Fig. 10 (a)). Similar to the NP1 model,

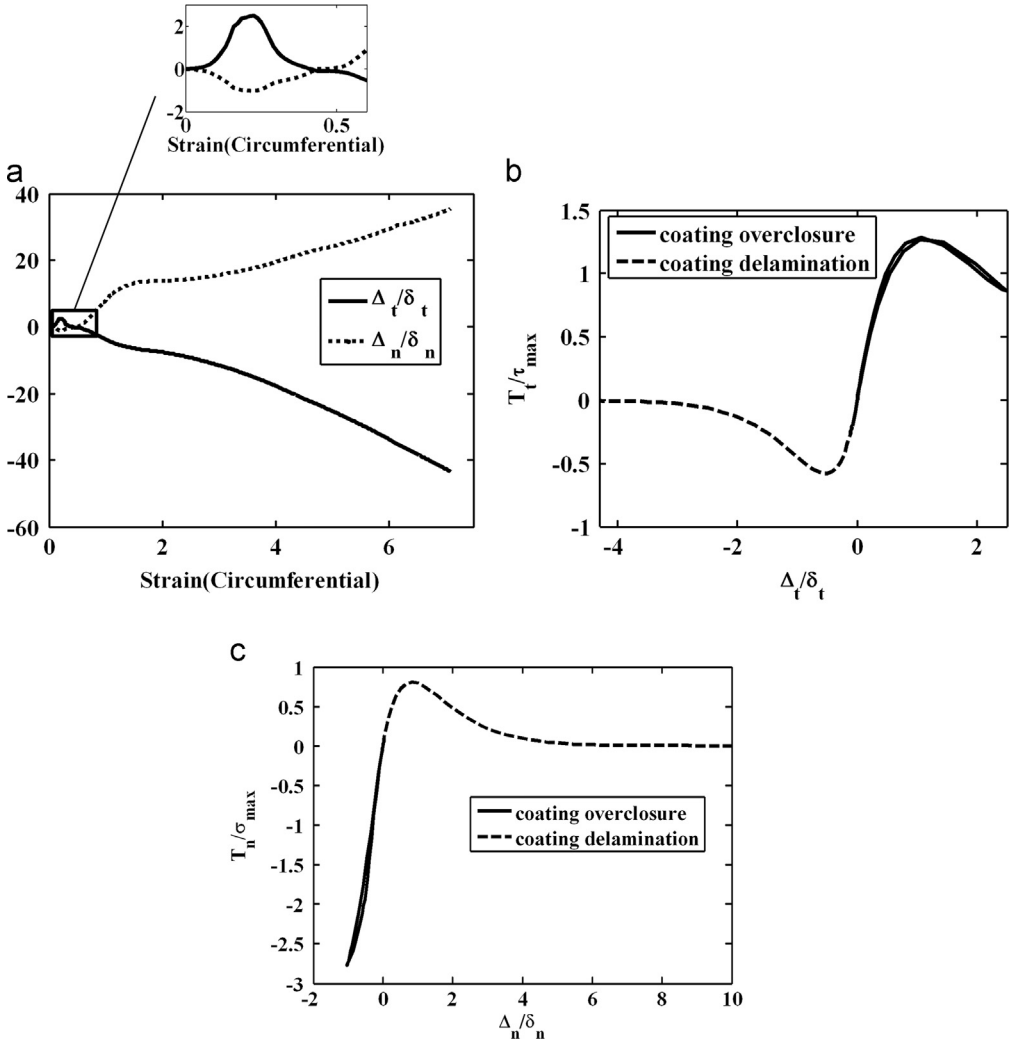

Fig. 10. Interface behaviour computed at point B during stent deployment using NP2: (a) Normal (Δ_n/δ_n) and tangential (Δ_t/δ_t) separation as a function of circumferential strain and (b) Tangential traction (T_t/τ_{max}) as a function of tangential separation (Δ_t/δ_t) and (c) Normal traction (T_n/σ_{max}) as a function of normal separation (Δ_n/δ_n).

tangential traction increases during mixed-mode over-closure, increasing the resistance to tangential separation. When normal over-closure reduces with the onset of coating buckling a peak tangential traction of $T_t/\tau_{max} \approx 1.25$ is computed (Fig. 10 (b)). While this value is lower than that the peak tangential traction computed by the NP1 model, mixed-mode over-closure is successfully penalised and coating buckling is predicted at higher stent deployment, as is evident in the normal traction–separation plot of Fig. 10 (c). It should be noted that separation is monotonic in Figs. 9 and 10 (with load reversal occurring only in the over-closure regime), ensuring that the non-potential formulations NP1 and NP2 provide instantaneous positive dissipation during coating debonding, as discussed in Part I of this study.

Fig. 11 shows the vonMises stress distribution on the deformed stent-coating geometry at a circumferential strain of 0.6 computed using NP1 and BSG formulations (Fig. 11(a) and (b) respectively). Figure inserts show details of the deformed stent and coating geometry in the region of point B. Using the NP1 model, mixed-mode over-closure of the coating is correctly penalised in the compressive region of the stent. The prevention of mixed-mode over-closure results in the computation of a highly stressed region in the coating to the right of point B which results in buckling of the coating from the stent surface. As deployment continues, the buckled region of the coating extends to point B and it separates from the stent surface, as discussed in relation to Fig. 9. In contrast to the NP1 model, the BSG model computes excessive mixed-mode over-closure at point B. As a result stresses in the coating are significantly reduced and buckling of the coating is not correctly predicted by the model as shown in Fig. 11(b).

As shown in Fig. 12(a), buckling of the coating from the stent surface becomes very pronounced at high levels of stent deployment (circumferential strain of 7.0) for the NP1 model. Such coating buckling during stent deployment has been observed experimentally (Basalus and von Birgelen, 2010). As demonstrated in Figs. 9–11, the ability of a CZM to predict such buckling is dependent on correct treatment of mixed-mode over-closure. Fig. 12(b) demonstrates that a similar pattern of buckling is computed by the NP2 model. Simulations were also performed using the SMC formulation in separation and

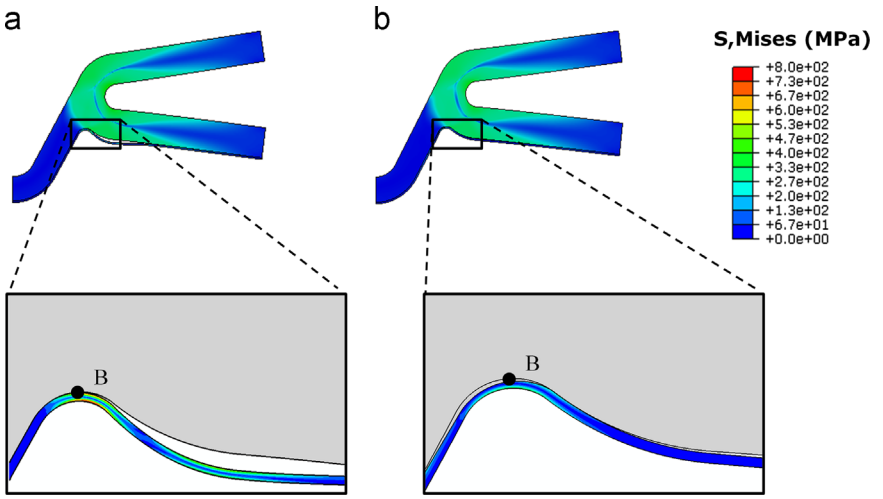

Fig. 11. Coating stress distribution plotted on the deformed geometry at a stent circumferential strain of 0.6: (a) NP1 model; (b) BSG model. Inserts illustrate that significant overclosure is computed by the BSG model resulting in decreased coating stress and decreased buckling of the coating.

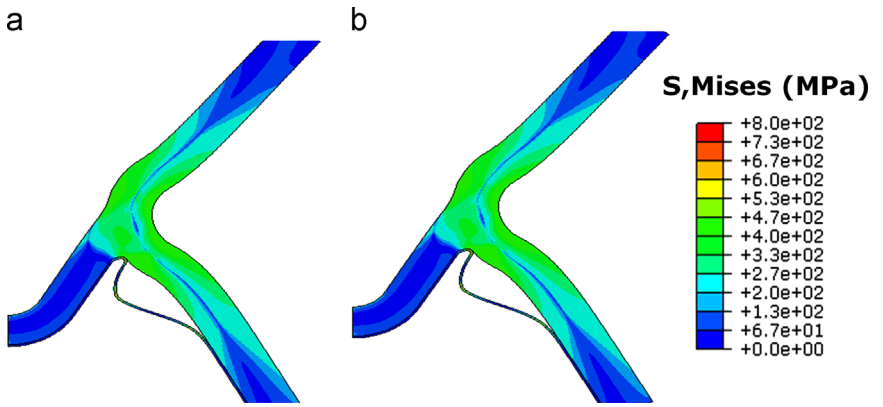

Fig. 12. Stent stress distribution plotted on the deformed geometry at a stent circumferential strain of 7 for (a) NP1 and (b) NP2. Significant buckling of the coating from the stent geometry is computed for both models.

NP2 formulation in over-closure and predicted results were very similar to those shown in Fig. 12(a) and (b). The ability of a CZM to predict coating buckling is critical for the safe design of coated stents, as demonstrated by the patterns of stent coating buckling shown in Fig. 13.

2.3. Case study III-composite circular arch delamination

Laminated composite circular arches are used in numerous applications. As structural members in the aerospace and marine sectors, they are appreciated for their high strength to weight ratio. This structural element is also typical of stents. The problem of multilayer circular arch deformation has been investigated within the framework of beams (Chandrashekhara and Rao, 1996; Matsunaga, 2003; Malekzadeh, 2009), using different kinematic models in order to estimate the stress distribution in the structure. An exact solution derived in the framework of two dimensional linear elasticity has been recently established (Parry and McGarry, 2012). Such a solution is of great importance to describe the normal and shear stress components at the interface between the two materials composing the arch.

The different CZMs are here examined in the case of the semi-circular arch subjected to prescribed displacements,U, at its base. The analytical solution provides the interface tractions prior to delamination. A representation of the arch is provided in Fig. 14. A polar coordinate system (variables , θ) is used. The interface is located at $r=R$ and the symmetry axis is also highlighted. The entire semi-circular arch is modelled to avoid computational problems which occur when a quarter-circular model is implemented; a normal traction singularity is computed at the top of the arch ($\theta=0$). Additionally, a multi

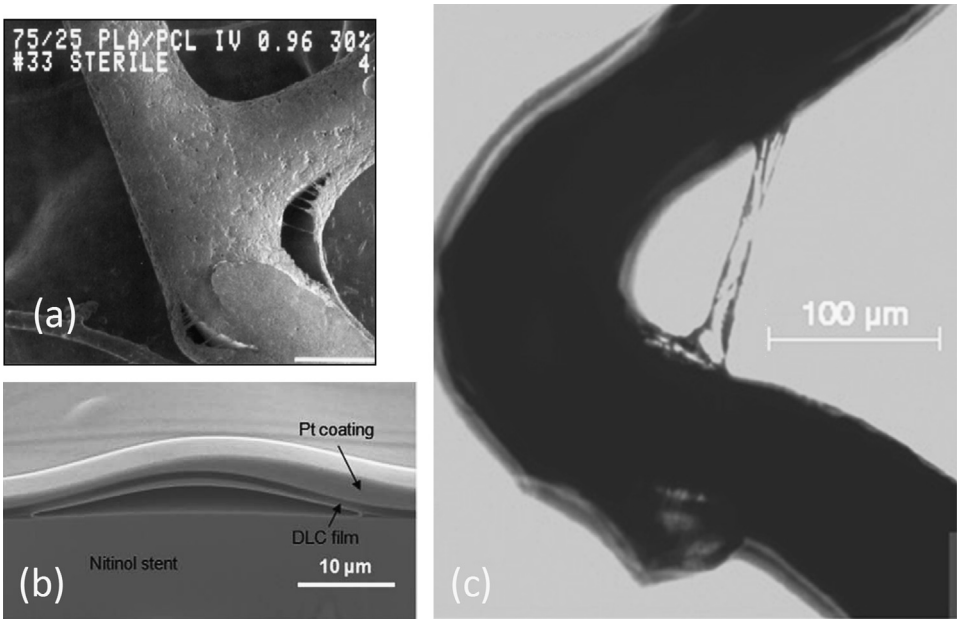

Fig. 13. Experimental images of stent coating buckling adapted from (a) Regar et al. (2001), (b) Kim et al. (2008) and (c) Basalus and von Birgelen (2010). It should be noted that in addition to coating buckling in compressive regions of the stent surface, (a) and (c) also show regions of coating delamination in tensile regions of the stent surface. This failure mechanism has not been investigated elsewhere (Hopkins et al., 2010; Parry and McGarry, 2012).

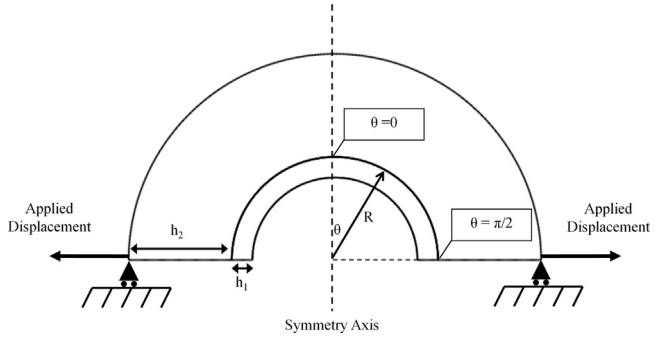

Fig. 14. Geometry of the arch and coating. Boundary conditions and applied displacements are highlighted. A polar co-ordinate system is used where R is the distance to the interface. Interface tractions and displacements are computed along the interface from $\theta=0$ to $\theta=\pi/2$.

point constraint slider boundary condition is implemented in the region at the bottom of the arch ($\theta = \pi/2$) in an effort to avoid associated computational problems in this region.

The coating material and the substrate materials are identified as layers 1 and 2, of thickness h_1 and h_2 respectively. The interface radius is denoted as R and applied displacement is denoted as U. An analytical solution for the stress state in the arch has been developed by Parry and McGarry (2012). Tractions along the interface can be obtained from the analytical solution:

$$\frac{T_t(\theta)}{\mu_1} = A\ \cos(\theta)\frac{U}{R} \tag{4}$$

$$\frac{T_n(\theta)}{\mu_1} = -A\ \sin(\theta)\frac{U}{R} \tag{5}$$

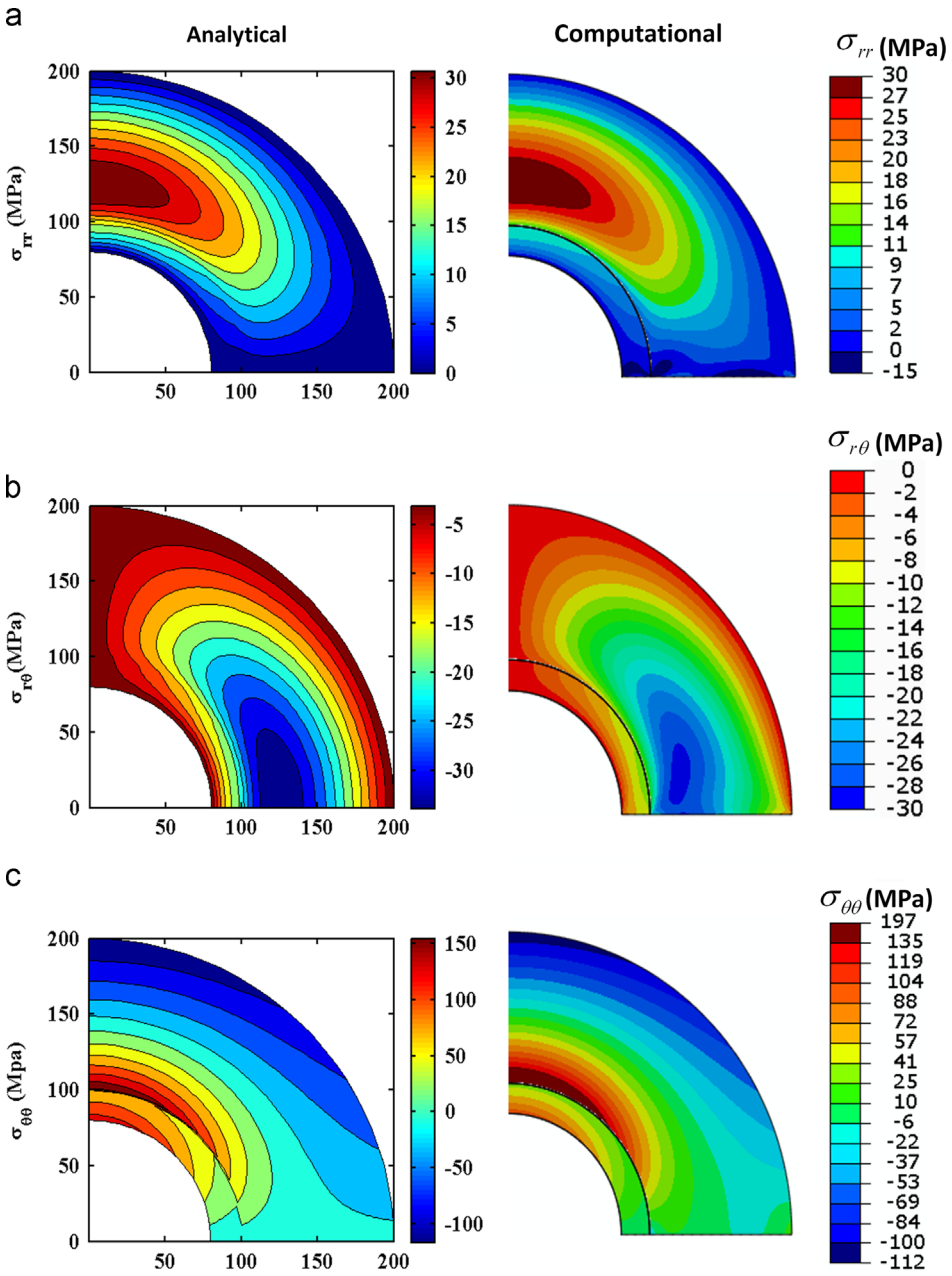

Fig. 15. Stress distribution plotted on the deformed geometry prior to coating delamination ($U/R = 1.014 \times 10^{-3}$). Comparison is made between analytical and finite element predictions for (a) normal stress (σ_{rr}); (b) shear stress ($\sigma_{r\theta}$) and (c) hoop stress ($\sigma_{\theta\theta}$). $h_2/R = 1$, $\kappa_1 = 1.8$, $\kappa_2 = 1.8$, $\mu_2/\mu_1 = 2.5$.

where the constant, A, is a function of the geometric and material parameters of the bi-layered arch. μ_1 and μ_2 are the shear moduli of layers 1 and 2, respectively. It is worth noting that the traction magnitude $\left(T_{mag}=\sqrt{{T_n}^2+{T_t}^2}\right)$ is constant along the interface. In order to predict the delamination of the structure, finite element calculations are carried out with the different CZMs. Firstly, in order to confirm the ability of the finite element model to replicate the analytical solution, a set of calculations is carried out, for which a very small prescribed displacement, U, is applied, so that the decohesion remains negligible (T_{eff} remains very small compared to the peak value). Cohesive zone parameters are chosen so that interface tractions are an order of magnitude lower than the interface strength i.e. the interface behaviour is in the elastic regime and no debonding occurs. Additionally interface characteristic lengths are chosen so that the interface stiffness is several orders of magnitude stiffer than the arch materials. Contour plots of the radial stress $\sigma_{rr}(r,\theta)$, shear stress $\sigma_{r\theta}(r,\theta)$ and the hoop stress $\sigma_{\theta\theta}(r,\theta)$ are reported in Fig. 15. This plot shows how stresses are distributed inside the coating prior to delamination. The finite element calculation shows very good agreement with the analytical solution, except for a small neighbourhood around the singular point at the base of the arch between the two materials ($r=R,\ \theta=\pi/2$).

2.3.1. Debonding simulations

Next, the XN, BSG, NP1, NP2, and SMC CZMs are used to predict debonding of the bi-layered arch. The elastic solution suggests that the interface provides a traction-dependent mode mixity. The mode angle depends on the coordinate along the interface, varying sinusoidally from pure mode II at the base of the arch to pure mode I at the top of the arch. It is worth noting that the analytical elastic solution does not include delamination, hence it is not directly comparable to the numerical CZM results over the full range of each simulation. However, as the analytical solution demonstrates perfect symmetry between the sinusoidal distributions of normal and tangential tractions along the arch interface, this case study provides a platform to uncover a bias towards normal or tangential delamination under mixed-model loading conditions due to the CZM coupling terms. Unless otherwise stated, cohesive zone parameters are chosen for the following analyses so that peak mode I traction and peak mode II tractions are equal ($\sigma_{max}=\tau_{max}$), with the peak occurring the same effective separation in mode I and mode II separation. The variations of T_n and T_t along the interface at the onset of debonding are reported in Fig. 16 (a)–(d) for the different CZMs, in addition to the analytical solution as a reference.

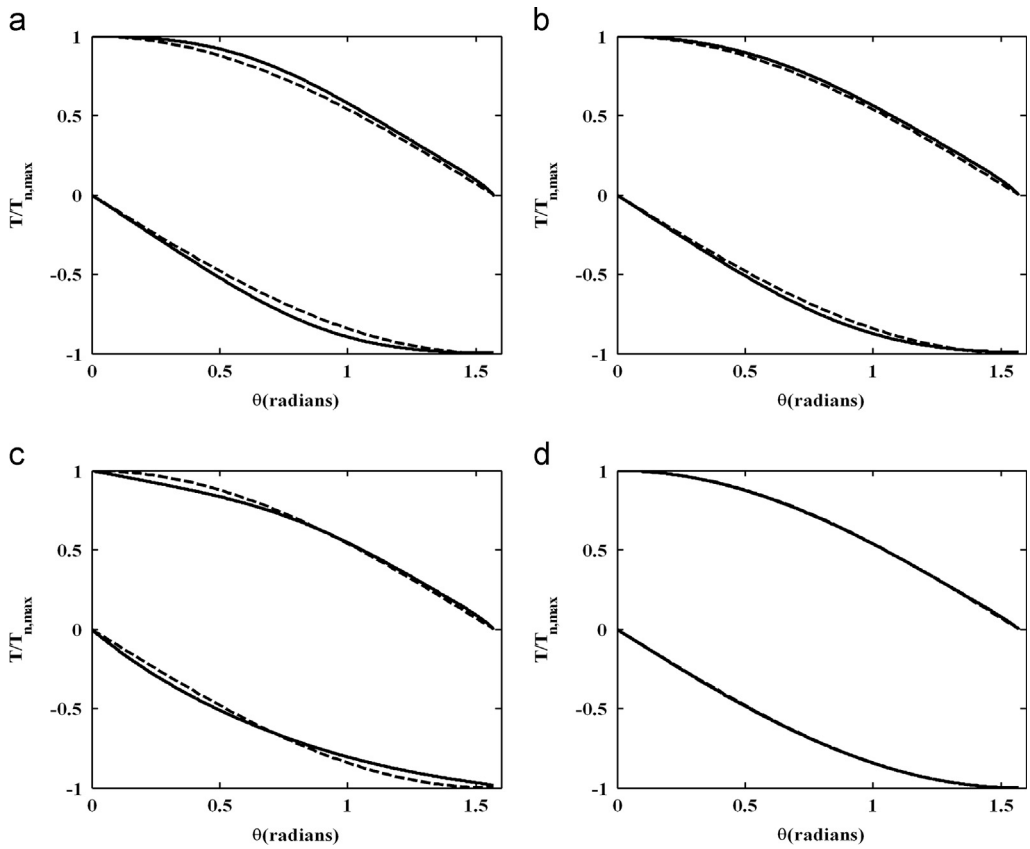

Fig. 16. Traction ($T/T_{n,max}$) computed at the bilayered arch interface for (a) XN model; (b) BSG model; (c) NP2 model and (d) SMC model at arch deployment where $T_n=T_{n,max}$ at $\theta=0$. Computational curves are solid lines whereas analytical curves are dotted lines.

The traction distribution in all the different models follow the pattern indicated by the analytical solution, namely a tensile normal traction T_n increasing from $T_n = 0$ at the bottom ($\theta = \pi/2$) to a maximum value at top ($\theta = 0$). Also, as expected, the absolute value of the shear traction Tt is maximum at the bottom of the arch and decreases with increasing θ, vanishing at the top. The XN model is examined in Fig. 16(a). The results are mediocre, except for pure mode I ($\theta = 0$) and pure mode II ($\theta = \pi/2$). The largest gap to the analytical result appears to be around $\theta = \pi/4$, where the analytical solution enforces that $||T_n|| = ||T_t||$. Results for the BSG model presented in Fig. 16(b) show similar characteristics, although the maximum distance between numerical and analytical results seems to be lower than for the XN model. Results for NP2 $\left(\alpha = \beta = \left(\sqrt{2}-1\right)\right)$ are depicted Fig. 16(c). This model matches exactly the analytical solution for $\theta = 0$, $\theta = \pi/4$ and $\theta = \pi/2$. However, a clear difference with the analytical model appears for the intermediate values. Finally, Fig. 16(d) reveals that the SMC formulation provides a very good match with the analytical solution. Clearly, for a given point along the interface, the analytical solution for the interface stress will be all the better reproduced if the cohesive zone stiffness is high compared to the stiffness of the surrounding materials. This condition is fulfilled by all the models, since the relative difference between the numerical solution and the analytical solution does not exceed 8%. Nevertheless a good agreement with the analytical solution is not attained at every point of the interface for a given model except for the SMC formulation.

Fig. 17 shows the normal (Δ_n) and tangential (Δ_t) displacements computed at 21 equally distributed nodes along the bi-layered arch interface during arch deployment. The lines coincident with the x and y-axis are the computed displacement at the bottom ($\theta = \pi/2$) and top ($\theta = 0$) of the arch respectively. Lines indicating proportional separation at $\theta = \pi/8$, $\pi/4$ and $3\pi/8$ are shown in order to compare with computed displacements at these points along the interface. The displacements at the interface occur in such a way as to maintain a constant traction ratio (T_n/T_t) until the peak traction magnitude ($|T|_{max} = \max(\sqrt{T_n^2+T_t^2})$) is reached. CZM model parameters are chosen so that the peak mode I and mode II tractions are equal (i.e. $|T|_{max}^{\theta=0} = |T|_{max}^{\theta=\pi/2}$) and the separation magnitude at which these peak tractions occur are also equal (i.e. $|\Delta|_{max}^{\theta=0} = |\Delta|_{max}^{\theta=\pi/2}$). However, as discussed in Part I of this study, the form of the traction–separation curves are different for mode I and mode II separation for NP1, BSG and XN models.

Considering firstly the XN CZM (Fig. 17(a)), in order to maintain a constant traction ratio, the form of the equations dictate that the interface displacements tend toward a mode I type separation for $0 \le \theta \le \pi/4$. A reasonable agreement is computed at $\theta = \pi/8$ between the computed displacement ratio and the displacement ratio required for proportional

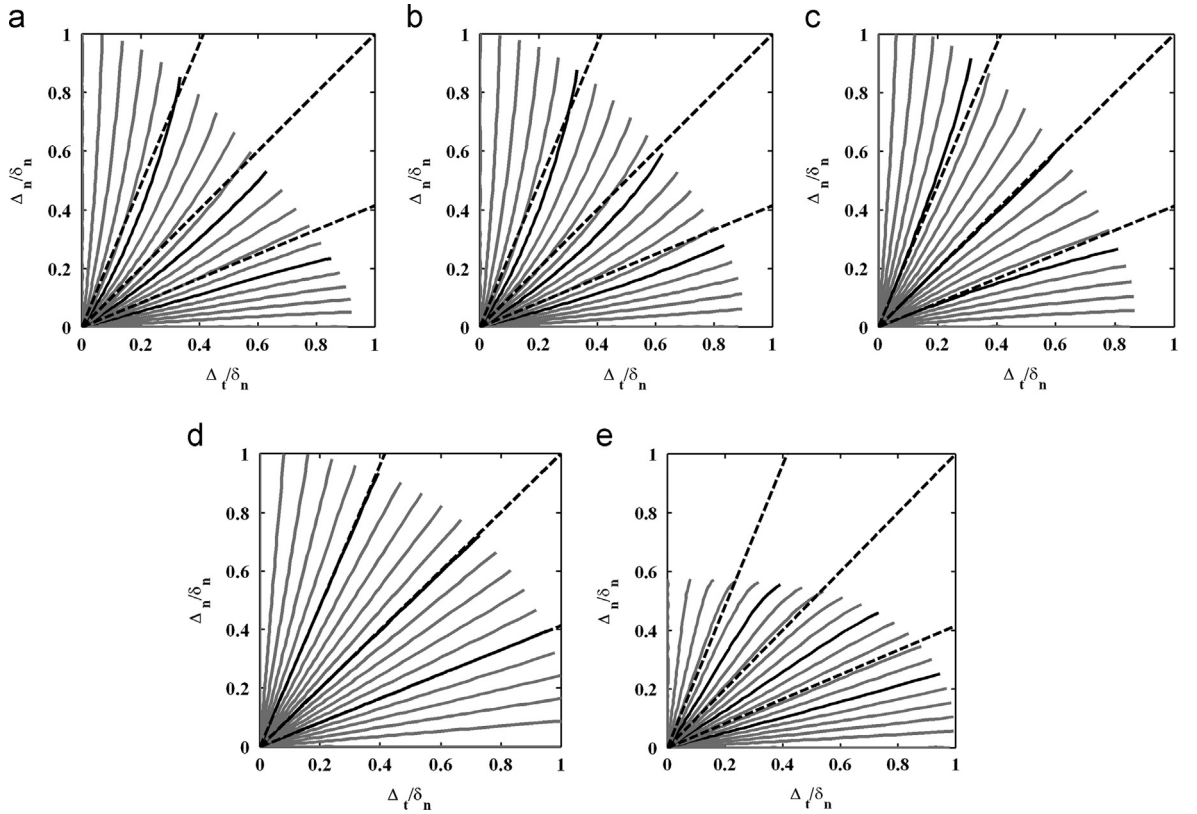

Fig. 17. Separation paths [Δ_n/δ_n versus Δ_t/δ_n] for 21 equally spaced nodes along the bilayered arch interface for (a) XN model (b) BSG model; (c) NP2 model; (d) SMC model and (e) NP1 model at an arch deployment where the peak traction magnitude ($|T|_{max}$) is reached. Proportional loading paths at $\theta = \pi/8$, $\pi/4$ and $3\pi/8$ are indicated by dotted lines.

loading. However, it is worth noting that there is a slight tendency towards mode II type separation for $\theta \geq 3\pi/8$. The BSG CZM predicts a slight tendency toward mode I separation for all points along the interface (Fig. 17(b)). In the case of the NP2 model (Fig. 17(c)), separation paths tend toward mode I for $0 \leq \theta < \pi/4$ and towards mode II type separation for $\theta > \pi/4$. Proportional displacement is computed a $\theta = \pi/4$ as expected. Using the SMC CZM (Fig. 17(d)), proportional displacement is computed at all points along the interface. Finally, for the NP1 model (Fig. 17(e)), mixed-mode separation paths tend towards the mode II axis. The peak traction magnitude is initially reached at $\theta \approx 0.3\pi$, followed by mode II dominated debonding characterised by increasing tangential separation.

The normal traction computed at the top of the arch ($\theta = 0$) and the tangential traction computed at the base of the arch ($\theta = \pi/2$) are shown in Fig. 18 for the XN, BSG, NP2 and SMC CZMs. With the exception of the SMC model, the normal traction exceeds the tangential traction as arch displacement is increased, with a peak normal traction being computed at $U/R \approx 2.4 \times 10^{-3}$, followed by interface delamination. In the case of the SMC model, the normal and tangential tractions are equal up to and beyond the peak, which occurs at a higher arch displacement of $U/R \approx 2.6 \times 10^{-3}$. Corresponding interface separations are shown in Fig. 19 (normal separation at $\theta = 0$ and tangential separation at $\theta = \pi/2$). In the case of the XN and BSG models the normal separation is initially lower than the tangential separation. However, as arch displacement increases the normal separation at the top of the arch exceeds the tangential separation at the bottom of the arch as the peak traction is approached. This results from the different forms of the mode I and mode II traction–separation relationships in the case of the XN and BSG CZMs. Following the peak traction at $U/R \approx 2.4 \times 10^{-3}$, the normal separation at the top of the arch increases rapidly. In the case of the NP2 CZM, as the form of the mode I and mode II traction–separation relationships are identical, the normal separation is equal to the tangential separation during initial arch displacement. However, similar to the XN and BSG simulations, the normal separation increases rapidly following the peak traction at $U/R \approx 2.4 \times 10^{-3}$, again leading to a mode I delamination of the arch. In the case of the SMC model, normal and tangential separations are identical up to and beyond the peak ($U/R \approx 2.6 \times 10^{-3}$). At $U/R \approx 2.8 \times 10^{-3}$ a bifurcation point is reached and tangential separations increase rapidly.

Fig. 20(a) and (b) show the deformed shape of the arch with contour plots of von Mises stress for SMC and XN models prior to the initiation of debonding . Displacements fields are amplified by a factor 100 for better visualisation. Similar stress

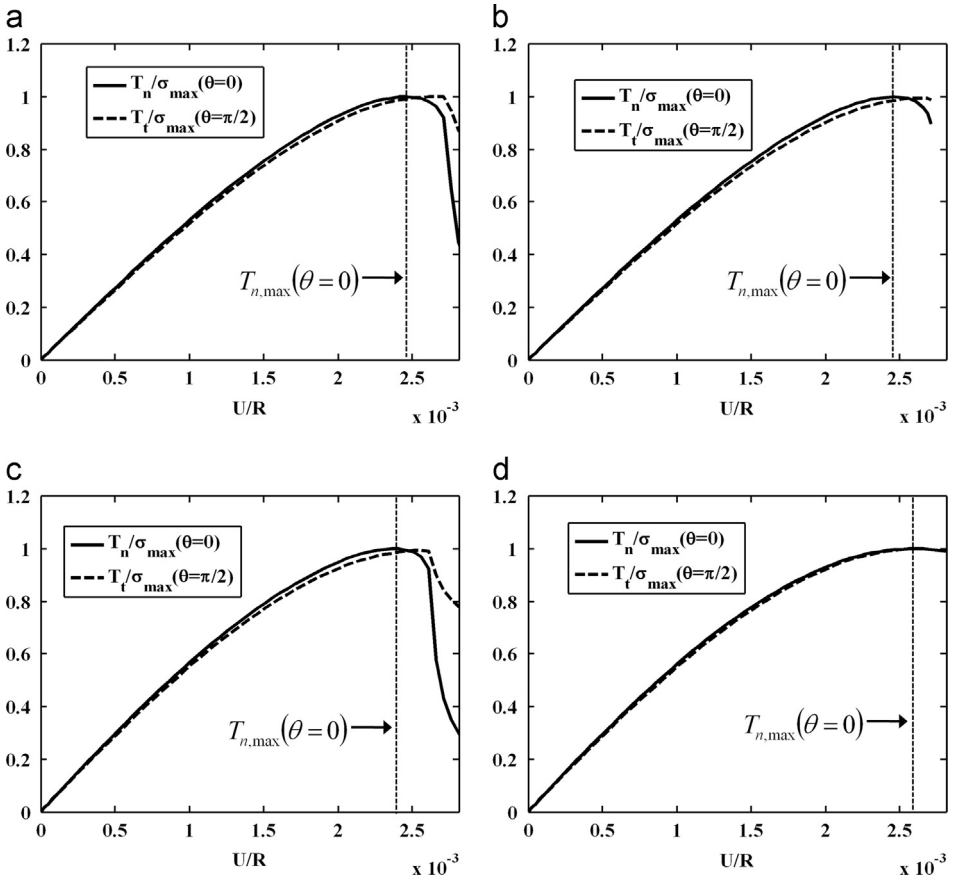

Fig. 18. Normal traction (T_n/σ_{max}) and tangential traction (T_t/σ_{max}) computed at the bilayered arch interface as a function of arch deployment (U/R) for (a) XN model; (b) BSG model; (c) NP2 model and (d) SMC model. Normal traction is computed at the top of the arch ($\theta = 0$) and tangential traction is computed at the bottom of the arch ($\theta = \pi/2$). The deployment at which maximum normal traction ($T_{n,max}$) is computed at the top of the arch ($\theta = 0$) is also indicated.

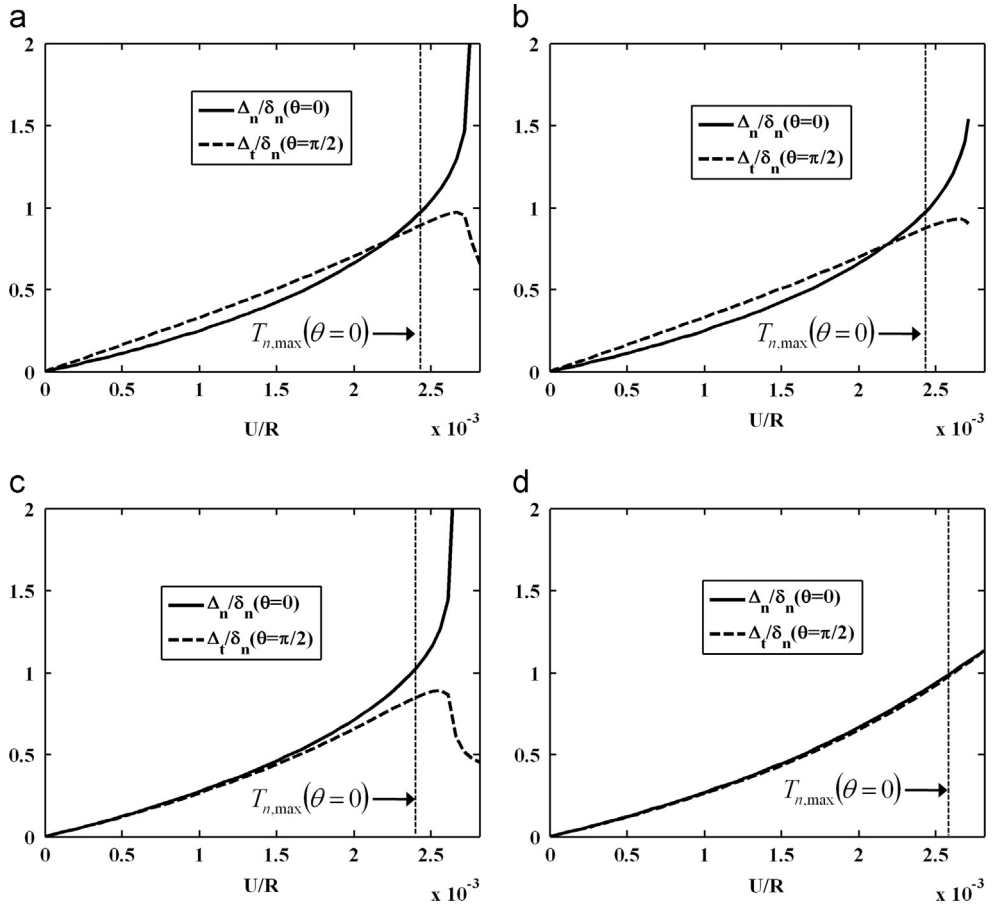

Fig. 19. Normal displacement (Δ_n/δ_n) and tangential displacement (Δ_t/δ_n) computed at the bilayered arch interface as a function of arch deployment (U/R) for (a) XN model; (b) BSG model; (c) NP2 model and (d) SMC model. Normal displacement is computed at the top of the arch ($\theta=0$) and tangential displacement is computed at the bottom of the arch ($\theta=\pi/2$). The deployment at which maximum normal traction ($T_{n,max}$) is computed at the top of the arch ($\theta=0$) is also indicated.

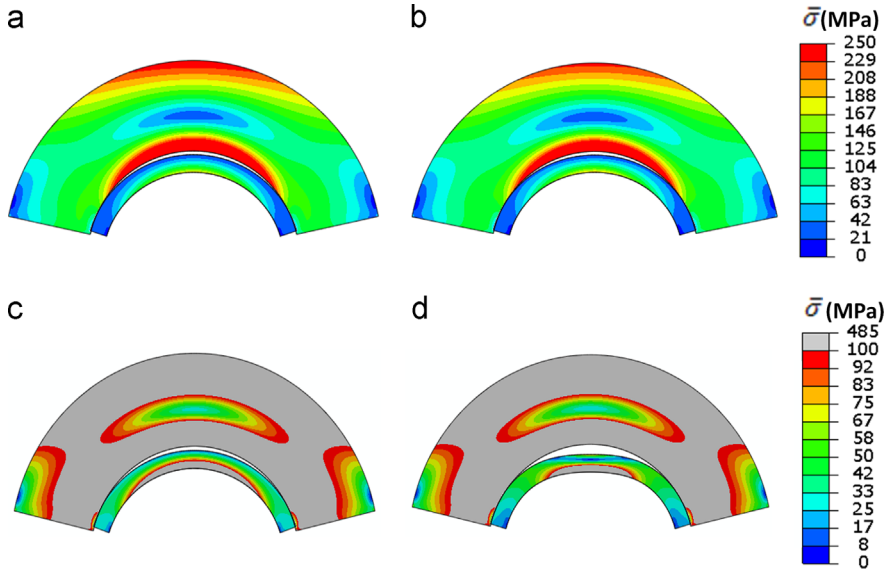

Fig. 20. von Mises stress distribution ($\bar{\sigma}$) plotted on the deformed geometry at arch deployment where $T_n=T_{n,max}$ at $\theta=0$ for (a) SMC model and (b) XN model. Computed von Mises stress distribution at arch deployment following the initiation of debonding at $\theta=0$; $T_n<T_{n,max}$; ($U/R=2.814\times10^{-3}$) for (c) SMC model and (d) XN model. Scale 1:100.

fields are computed in both layers (substrate and coating) of the arch. It should also be noted that the magnitude of mode I separation at the top of the arch and model II separation at the bottom of the arch are similar (as revealed in Fig. 19). However, following the initiation of debonding ($U/R \approx 2.8 \times 10^{-3}$) the coating is strained very differently in the case of the XN and SMC CZMs (Fig. 20(c) and (d)). Mode I separation at the top of the arch dominates when the XN CZM is used (and indeed when the BSG and NP2 CZMs are used, as shown in Fig. 19). In contrast, the SMC model predicts a gradual transition from mode I at the top of the arch to mode II at the bottom of the arch.

At a glance, the mode I dominance of the XN and BSG simulations is somewhat surprising, given that the work of mode I separation (ϕ_n) is greater that the work of mode II separation (ϕ_t) when $\sigma_{max} = \tau_{max}$ for these formulations. However, the analytical solution of Parry and McGarry (2012) demonstrates that the arch interface provides traction controlled mode mixity, with $\theta = Tan^{-1}(T_n/T_t)$. It should be recalled that in Part I of this study it was demonstrated that the XN and BSG models provide a strong bias towards normal separation under such conditions. Finite element predictions of separation paths along the arch interface for the XN model shown in Fig. 21(a) demonstrate a similar pattern of normal delamination to that observed theoretically in Part I. Following initiation of debonding the stress in the arch deviates from the analytical elastic solution so that traction controlled mode mixity is no longer enforced. At this point, tangential separations near the bottom of the arch are reversed as normal debonding dominates. A similar pattern is predicted using the NP2 CZM at the arch interface (Fig. 21(b)), again resembling the theoretical curves presented in Part I, including the prediction of an "exclusion zone" in which no separation paths occur.

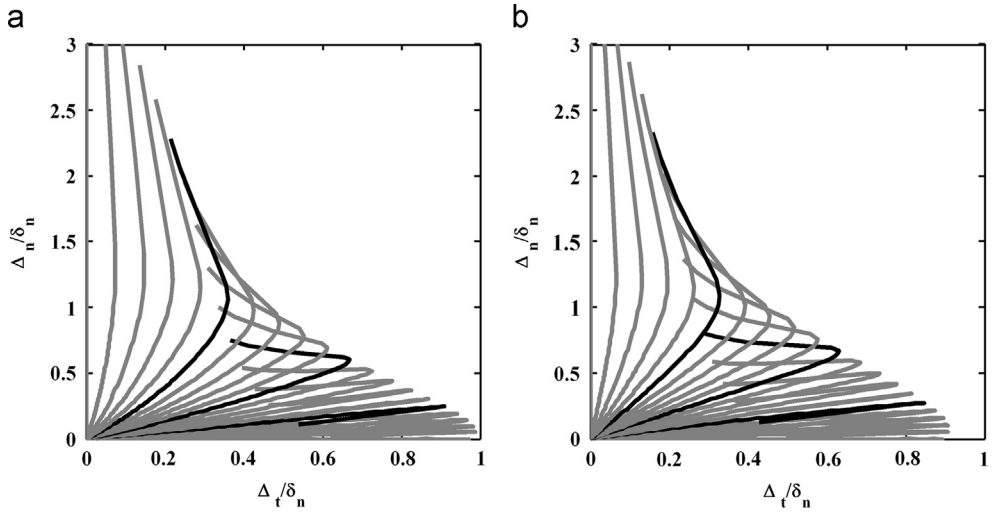

Fig. 21. Separation paths [Δ_n/δ_n versus Δ_t/δ_n] for 21 equally spaced nodes along the bilayered arch interface for (a) XN model (b) NP2 model. ($\sigma_{max} = \tau_{max} = 20\ MPa$).

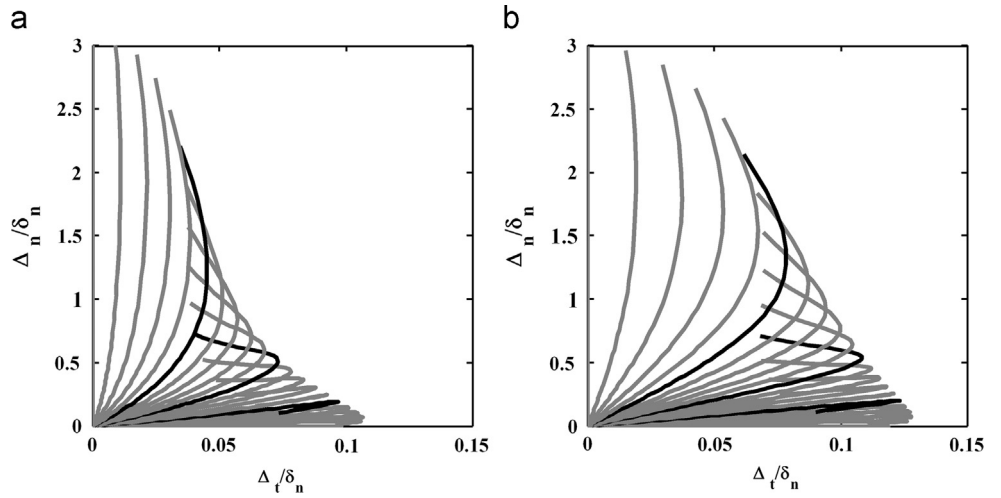

Fig. 22. Separation paths [Δ_n/δ_n versus Δ_t/δ_n] for 21 equally spaced nodes along the bilayered arch interface for (a) XN model (b) SMC model ($\phi_t = 4\phi_n$).

A final pair of simulations is presented in Fig. 22 where $\phi_t = 4\phi_n$ for both the XN (Fig. 22(a)) and SMC (Fig. 22(b)) models. As expected, mode I delamination at the top of the arch dominates in both cases. However, the mode mixity along the interface is quite different for both models, with the XN predicting separation paths that lie much closer to the pure mode *I* axis. Again, this finite element prediction is consistent with the theoretical analysis presented in Part I of this study. Finally, while a small degree of load reversal is computed in the bi-layered arch, positive instantaneous dissipation is computed at all points on the interface.

3. Concluding Remarks

In Part I of this two part study, theoretical analyses of the mixed-mode behaviour of potential-based and non-potential-based CZMs were presented, whereby an alternative potential-based CZM and three alternative non-potential-based CZMs were proposed. Theoretical analysis demonstrated several advantages of these formulations over the existing XN potential-based model and the BSG non-potential-based model. In Part II of this study, three finite element case studies were implemented to demonstrate the importance of the theoretical findings presented in Part I.

- The first case study presents the use of an interface potential to simulate the debonding and rebonding of a cell from a cyclically deforming substrate when the mode II work of separation is higher than the mode I work of separation. Using the commonly implemented XN potential, non-physical repulsive normal tractions are computed during the unloading half cycles, preventing readhesion of significant regions of the cell to the substrate. The computation of such non-physical repulsive tractions is avoided when the new MP model is implemented, allowing for the prediction of cytoskeletal realignment that corresponds closely to experimental observation (Wang et al., 1995; Wang et al., 2001; Kaunas et al., 2005). Residual tractions are unavoidable for potential-based CZMs if $\phi_t \neq \phi_n$, but this case study demonstrates the effectiveness of the MP model in reducing the separation field in which residual tractions occur.
- The second case study entails the use of non-potential-based models to simulate coating buckling from the compressive region of a stent during deployment. The previously proposed BSG CZM fails to correctly penalise mixed-mode over-closure at the compressive region of the stent surface, predicting an unphysical penetration of coating into the stent surface. Such over-closure has a pronounced influence on computed stresses in the coating and extensive coating buckling is not predicted. In contrast, the new NP1 and NP2 CZMs correctly penalise mixed-mode over-closure, leading to significant buckling of the coating as stent deployment is increased. Such coating buckling has been observed in benchtop testing of coated stents (Basalus and von Birgelen, 2010; Regar et al., 2001). This case study clearly demonstrates that a CZM must correctly penalise mixed-mode over-closure in order to predict coating buckling.
- The third case study entails the simulation of the delamination of a bi-layered arch when a horizontal displacement is applied to the arch base. The previously developed analytical solution of Parry and McGarry (2012) demonstrates that in the elastic regime, prior to debonding, the arch interface enforces traction controlled mode mixity, with the ratio of normal to tangential traction depending exclusively on position along the interface. Finite element simulations reveal that the XN, BSG and NP2 models provide a significant bias towards mode I delamination when $\sigma_{max} = \tau_{max}$. The NP1 model provides a very weak resistance to mixed-mode delamination in comparison to pure mode I or pure mode II delamination. The weakest point on the interface occurs at $\theta \approx 0.3\pi$, and following initiation at this point the coating undergoes primarily tangential delamination at the bottom of the arch. The SMC model provides mode-independent behaviour up to and beyond the initiation of debonding. This case study demonstrates the importance of normal-tangential coupling terms in CZMs for mode-sensitive traction controlled conditions, as suggested by the theoretical analyses presented in Part I of this study.

In conclusion, the present study uncovers a number of inherent problems in potential-based and non-potential-based CZMs under mixed-mode separation and over-closure. A number of new models (MP, NP1, NP2 and SMC) are proposed in an attempt to overcome such problems. The first case study demonstrates the advantages of the MP model over the XN model. The second case study demonstrates the advantage of the new non-potential-based CZMs over the BSG model for problems in which mixed-mode over-closure may be encountered. The third case study highlights the sensitivity of CZMs to traction controlled mode mixity. Previous papers have typically used double cantilever beam data with uneven bending moment to validate cohesive zone performance under mode I and mixed-mode conditions (Sørensen and Jacobsen, 2003; van den Bosch et al., 2006; Park et al., 2009; Mosler and Scheider, 2011). The three case studies presented in this paper provide further challenges in the assessment of mixed-mode cohesive zone performance and should be considered in addition to double cantilever beam simulation.

Acknowledgements

This work was supported by Science Foundation Ireland (Grant no. 08/RFP/ENM1726). JPMcG and GP acknowledge an IRCSET ULYSSES/Egide travel grant. The authors wish to acknowledge the SFI/HEA Irish Centre for High End Computing (ICHEC) for the provision of computational facilities and support. The authors thank Robert M. McMeeking, Vikram S. Deshpande and William Ronan for ongoing development of 3D cell contractility models.

Reference

Abdul-Baqi, A., Van Der Giessen, E., 2001. Indentation-induced interface delamination of a strong film on a ductile substrate. Thin Solid Films 381, 143–154.

Asaoka, K., Kuwayama, N., Okuno, O., Miura, I., 1985. Mechanical properties and biomechanical compatibility of porous titanium for dental implants. J. Biomed. Mater. Res. 19, 699–713.

Babapulle, M.N., Eisenberg, M.J., 2002. Coated stents for the prevention of restenosis: part I. Circulation 106, 2734–2740.

Balestrini, J.L., Skorinko, J.K., Hera, A., Gaudette, G.R., Billiar, K.L., 2010. Applying controlled non-uniform deformation for in vitro studies of cell mechanobiology. Biomech. Model. Mechanobiol. 9, 329–344.

Basalus, M.W.Z., Von Birgelen, C., 2010. Benchside testing of drug-eluting stent surface and geometry. Interv. Cardiol 2, 159–175.

Bell, G.I., 1978. Models for the specific adhesion of cells to cells. Science 200, 618.

Burridge, K., Chrzanowska-Wodnicka, M., 1996. Focal adhesions, contractility, and signaling. Annu. Rev. Cell Dev. Biol. 12, 463–519.

Caille, N., Thoumine, O., Tardy, Y., Meister, J.-J., 2002. Contribution of the nucleus to the mechanical properties of endothelial cells. J. Biomech. 35, 177–187.

Camacho, G.T., Ortiz, M., 1996. Computational modelling of impact damage in brittle materials. Int. J. Solids Struct. 33, 2899–2938.

Chan, B.P., Bhat, V.D., Yegnasubramanian, S., Reichert, W.M., Truskey, G.A., 1999. An equilibrium model of endothelial cell adhesion via integrin-dependent and integrin-independent ligands. Biomaterials 20, 2395–2403.

Chandrashekhara, K., Rao, K.S.N., 1996. Analysis of a long thick orthotropic circular cylindrical shell panel. J. Eng. Mech. 122, 575.

Dembo, M., Torney, D.C., Saxman, K., Hammer, D., 1988. The reaction-limited kinetics of membrane-to-surface adhesion and detachment. Proceedings of the Royal society of London. Ser. B, Biol. Sci., 55–83.

Deshpande, V.S., Mcmeeking, R.M., Evans, A.G., 2006. A bio-chemo-mechanical model for cell contractility. Proc. Ntl. Acad. Sci. 103, 14015–14020.

Deshpande, V.S., Mrksich, M., Mcmeeking, R.M., Evans, A.G., 2008. A bio-mechanical model for coupling cell contractility with focal adhesion formation. J. Mech. Phys. Solids. 56, 1484–1510.

Dong, C., Lei, X.X., 2000. Biomechanics of cell rolling: shear flow, cell-surface adhesion, and cell deformability. J. Biomech. 33, 35–43.

Dowling, E.P., Ronan, W., Ofek, G., Deshpande, V.S., Mcmeeking, R.M., Athanasiou, K.A., et al., 2012. The effect of remodelling and contractility of the actin cytoskeleton on the shear resistance of single cells: a computational and experimental investigation. J. R. Soc. Interface 9, 3469–3479.

Dowling, E.P., Ronan, W., McGarry, J.P., 2013. Computational investigation of in situ chondrocyte deformation and actin cytoskeleton remodelling under physiological loading. Acta Biomater. 9, 5943–5955.

Edelman, E.R., Seifert, P., Groothuis, A., Morss, A., Bornstein, D., Rogers, C., 2001. Gold-coated NIR stents in porcine coronary arteries. Circulation 103, 429.

Evans, E.A., 1985. Detailed mechanics of membrane-membrane adhesion and separation. I. Continuum of molecular cross-bridges. Biophys. J. 48, 175–183.

Franke, R.P., Grafe, M., Schnittler, H., Seiffge, D., Mittermayer, C., Drenckhahn, D., 1984. Induction of human vascular endothelial stress fibres by fluid shear stress. Nature. 307, 648–649.

Freund, L.B., Lin, Y., 2004. The role of binder mobility in spontaneous adhesive contact and implications for cell adhesion. J. Mech. Phys. Solids. 52, 2455–2472.

Hill, A.V., 1938. The heat of shortening and the dynamic constants of muscle. Proc. R. Soc. London Ser. B, Biol. Sci. 126, 136–195.

Hopkins, C.G., Mchugh, P.E., Mcgarry, J.P., 2010. Computational investigation of the delamination of polymer coatings during stent deployment. Ann. Biomed. Eng. 38, 2263–2273.

Hsu, H.J., Lee, C.F., Kaunas, R., 2009. A dynamic stochastic model of frequency-dependent stress fiber alignment induced by cyclic stretch. PloS one 4, e4853.

Hutchinson, J.W., Suo, Z., 1992. Mixed mode cracking in layered materials. Adv. Appl. Mech. 29, 191.

Kaunas, R., Nguyen, P., Usami, S., Chien, S., 2005. Cooperative effects of Rho and mechanical stretch on stress fiber organization. Proc. Ntl. Acad. Scie. USA 102, 15895.

Kim, H.-J., Moon, M.-W., Lee, K.-R., Seok, H.-K., Han, S.-H., Ryu, J.-W., et al., 2008. Mechanical stability of the diamond-like carbon film on nitinol vascular stents under cyclic loading. Thin Solid Films 517, 1146–1150.

Kolega, J., 1986. Effects of mechanical tension on protrusive activity and microfilament and intermediate filament organization in an epidermal epithelium moving in culture. J. Cell Biol. 102, 1400–1411.

Leckband, D., Israelachvili, J., 2001. Intermolecular forces in biology. Q. Rev. Biophys. 34, 105–267.

Malekzadeh, P., 2009. A two-dimensional layerwise-differential quadrature static analysis of thick laminated composite circular arches. Appl. Math. Modell. 33, 1850–1861.

Matsunaga, H., 2003. Interlaminar stress analysis of laminated composite and sandwich circular arches subjected to thermal/mechanical loading. Compos. Struct. 60, 345–358.

Mcgarry, J.P., Fu, J., Yang, M.T., Chen, C.S., Mcmeeking, R.M., Evans, A.G., et al., 2009. Simulation of the contractile response of cells on an array of micro-posts. Philos. Trans. R. Soc. A: Math. Phys. Eng. Sci. 367, 3477–3497.

Mcgarry, J.P., Mchugh, P.E., 2008. Modelling of in vitro chondrocyte detachment. J. Mech. Phys. Solids. 56, 1554–1565.

Mcgarry, J.P., Murphy, B.P., Mchugh, P.E., 2005. Computational mechanics modelling of cell-substrate contact during cyclic substrate deformation. J. Mech. Phys. Solids. 53, 2597–2637.

Mcgarry, J.P., O'donnell, B.P., Mchugh, P.E., Mcgarry, J.G., 2004. Analysis of the mechanical performance of a cardiovascular stent design based on micromechanical modelling. Comput. Mater. Sci. Surf. Eng. 31, 421–438.

Mcgarry, J.P., O'donnell, B.P., Mchugh, P.E., O'cearbhaill, E., Mcmeeking, R.M., 2007. Computational examination of the effect of material inhomogeneity on the necking of stent struts under tensile loading. J Appl Mech 74, 978.

Moretti, M., Prina-Mello, A., Reid, A.J., Barron, V., Prendergast, P.J., 2004. Endothelial cell alignment on cyclically-stretched silicone surfaces. J. Mater. Sci.: Mater. Med 15, 1159–1164.

Mosler, J., Scheider, I., 2011. A thermodynamically and variationally consistent class of damage-type cohesive models. J. Mech. Phys. Solids. 59, 1647–1668.

Na, S., Meininger, G.A., Humphrey, J.D., 2007. A theoretical model for F-actin remodeling in vascular smooth muscle cells subjected to cyclic stretch. J. Theor. Biol. 246, 87–99.

Needleman, A., 1987. A continuum model for void nucleation by inclusion debonding. J Appl. Mech. 54, 525–531.

Park, K., Paulino, G.H., Roesler, J.R., 2009. A unified potential-based cohesive model of mixed-mode fracture. J. Mech. Phys. Solids. 57, 891–908.

Parry, G., Mcgarry, P., 2012. An analytical solution for the stress state at stent-coating interfaces. J. Mech. Behav. Biomed. Mater. 10, 183–196.

Planas, J., Elices, M., 1993. Asymptotic analysis of a cohesive crack: 2. Influence of the softening curve. Int. J. Fract. 64, 221–237.

Regar, E., Sianos, G., Serruys, P.W., 2001. Stent development and local drug delivery. British Med. Bull. 59, 227.

Ronan, W., Deshpande, V.S., Mcmeeking, R.M., McGarry, J.P., 2012. Numerical investigation of the active role of the actin cytoskeleton in the compression resistance of cells. J. Mech. Behav. Biomed. Mater. 14, 143–157.

Ronan, W., Deshpande, V.S., Mcmeeking, R.M., McGarry, J.P., 2013. Cellular contractility and substrate elasticity: a numerical investigation of the actin cytoskeleton and cell adhesion. Biomech. Model. Mechanobiol. http://dx.doi.org/10.1007/s10237-013-0506-z. (In Press).

Sørensen, B.F., Gamstedt, E.K., Østergaard, R.C., Goutianos, S., 2008. Micromechanical model of cross-over fibre bridging-prediction of mixed mode bridging laws. Mech. Mater. 40, 220–234.

Sørensen, B.F., Jacobsen, T.K., 2003. Determination of cohesive laws by the J integral approach. Eng. Fract. Mech. 70, 1841–1858.

Sørensen, B.F., Jacobsen, T.K., 2009. Characterizing delamination of fibre composites by mixed mode cohesive laws. Compos. Sci. Technol. 69, 445–456.

Tan, J.L., Tien, J., Pirone, D.M., Gray, D.S., Bhadriraju, K., Chen, C.S., 2003. Cells lying on a bed of microneedles: an approach to isolate mechanical force. PNAS 100, 1484.

Thomopoulos, S., Fomovsky, G.M., Holmes, J.W., 2005. The development of structural and mechanical anisotropy in fibroblast populated collagen gels. J. Biomech. Eng. 127, 742.

Thoumine, O., Kocian, P., Kottelat, A., Meister, J.J., 2000. Short-term binding of fibroblasts to fibronectin: optical tweezers experiments and probabilistic analysis. Eur. Biophy. J. 29, 398–408.
Tvergaard, V. 1990. Effect of fibre debonding in a whisker-reinforced metal. Name: materials science and engineering, a: structural materials: properties, Microstruct. Process.
Tvergaard, V., Hutchinson, J.W., 1992. The relation between crack growth resistance and fracture process parameters in elastic-plastic solids. J. Mech. Phys. Solids. 40, 1377–1397.
Tvergaard, V., Hutchinson, J.W., 1993. The influence of plasticity on mixed mode interface toughness. J. Mech. Phys. Solids. 41, 1119–1135.
Ural, A., Krishnan, V.R., Papoulia, K.D., 2009. A cohesive zone model for fatigue crack growth allowing for crack retardation. Int. J. Solids Struct. 46, 2453–2462.
Van Den Bosch, M.J., Schreurs, P.J.G., Geers, M.G.D., 2006. An improved description of the exponential Xu and Needleman cohesive zone law for mixed-mode decohesion. Eng. Fract. Mech. 73, 1220–1234.
Wang, H., Ip, W., Boissy, R., Grood, E.S., 1995. Cell orientation response to cyclically deformed substrates: experimental validation of a cell model. J. Biomech. 28, 1543–1552.
Wang, J.H.C., Goldschmidt-Clermont, P., Wille, J., Yin, F.C.P., 2001. Specificity of endothelial cell reorientation in response to cyclic mechanical stretching. J. Biomech. 34, 1563–1572.
Warshaw, D.M., Desrosiers, J.M., Work, S.S., Trybus, K.M., 1990. Smooth muscle myosin cross-bridge interactions modulate actin filament sliding velocity in vitro. J. Cell Boil. 111, 453–463.
Weafer, P.P., Ronan, W., Jarvis, S.P., McGarry, J.P., 2013. Experimental and computational investigation of the role of stress fiber contractility in the resistance of osteoblasts to compression. Bull. Math. Biol. 75, 1284–1303.
Windecker, S., Mayer, I., De Pasquale, G., Maier, W., Dirsch, O., De Groot, P., et al., 2001. Stent coating with titanium-nitride-oxide for reduction of neointimal hyperplasia. Circulation 104, 928.
Xu, X.P., Needleman, A., 1993. Void nucleation by inclusion debonding in a crystal matrix. Modell. Simul. Mater. Sci. Eng. 2, 417–418.
Yan, Y., Shang, F., 2009. Cohesive zone modeling of interfacial delamination in PZT thin films. Int. J. Solids Struct. 46, 2739–2749.